remote sensing

MDPI

Article

Robust Satellite Techniques for Detecting and Monitoring Icebergs by Sentinel-2 Data

Iacopo Mancusi [1,2], Roberto Colonna [1,2,*], Carolina Filizzola [2,3], Nicola Genzano [2,4], Mariano Lisi [1,2] and Valerio Tramutoli [1,2]

[1] Department of Engineering, University of Basilicata, 85100 Potenza, PZ, Italy; iacopo.mancusi@unibas.it (I.M.); valerio.tramutoli@unibas.it (V.T.)
[2] Space Technologies and Application Centre, 85100 Potenza, PZ, Italy; carolina.filizzola@cnr.it (C.F.)
[3] Istituto di Metodologie Integrate per l'Osservazione della Terra (IMIOT), Consiglio Nazionale delle Ricerche (CNR), c/da S. Loja, 85050 Tito, PZ, Italy
[4] Department of Architecture, Built Environment and Construction Engineering (DABC), Politecnico di Milano, Via Ponzio 31, 20133 Milan, MI, Italy
* Correspondence: roberto.colonna@unibas.it

Highlights

What are the main findings?

- This study proposes a newly developed application of the RST for iceberg detection using Sentinel-2 data;
- The proposed method, differently from traditional fixed-threshold techniques, contemporarily guarantees high sensitivity (even for very small objects) and high reliability (against false positives) without requiring any preliminary adjustment or calibration.

What are the implications of the main findings?

- The proposed methodology provides a simple, reliable, automatic monitoring method for detecting icebergs, which could be particularly useful for providing timely warnings to vessels.
- Thanks to its intrinsic exportability (it requires only a multi-annual dataset of satellite images), this approach will allow iceberg detection across different geographical areas and different sensors.

Abstract

In recent decades, the sharp rise in global temperatures has accelerated the melting of the polar ice caps, causing icebergs to break off and subsequently drift across the sea surface. At the same time, the increase in navigable areas in the Arctic region has led to a continued growth in maritime traffic at higher latitudes, resulting in a consequent increase in the risk of iceberg–ship collisions. In this context, it is particularly important to provide vessels at sea with timely and up-to-date information on the presence of icebergs along routes in mid- and high-latitude waters. Given this challenge, this paper presents, for the first time, the Robust Satellite Techniques (RST) methodology employed at the global level to perform iceberg detection using imagery acquired only in the B3 band (centred at 560 nm) by the Sentinel-2 (S2) constellation. A test performed near Greenland (in September 2016) and in the Labrador Sea (in August 2021), showed that, in comparison with traditional fixed-threshold methods, this approach (easily implementable in the Google Earth Engine cloud platform) demonstrated: (a) very high sensitivity by doubling the number of detected icebergs (including the smaller ones); (b) high reliability with an overall false positive below 20% that becomes zero when other objects that may pose a hazard to navigation (e.g., dark ships, shallow reefs, etc.) are also considered.

Check for updates

Academic Editor: Hongyi Li

Received: 1 September 2026
Revised: 7 October 2026
Accepted: 12 October 2026
Published: 14 October 2026

Copyright: © 2026 by the authors. Licensee MDPI, Basel, Switzerland. This article is an open access article distributed under the terms and conditions of the Creative Commons Attribution (CC BY) license.

Keywords: arctic; iceberg; iceberg detection; Robust Satellite Techniques (RST); optical satellite data; Sentinel-2; Labrador Sea; Greenland; change detection

1. Introduction

Among the main consequences of climate change there is certainly the rise in temperatures, which leads to the melting of the polar ice caps in the Arctic and Antarctic regions [1], resulting in the formation of large ice blocks known as icebergs. Monitoring these objects is crucial for climate research, maritime safety and environmental management.

Icebergs vary greatly in shape and size, as well as in their drift speed and trajectories, which, depending on ocean currents, waves and wind [2,3], are difficult to predict and play a significant role within the marine ecosystems [4] at polar and subpolar latitudes due to their carbon release into the oceans [5], as well as having an impact on ocean circulation at local and global scales during their melting [6]. Furthermore, the release of fresh water by icebergs influences the distribution of sea ice, its thickness and total mass, with an indirect effect on their internal dynamics [7,8] and on Earth's surface albedo [9]. Monitoring and detecting drifting icebergs is also important, as they pose a threat to maritime safety, offshore activities and underwater pipeline systems in mid- and high-latitude regions [10,11]. In fact, in these regions, the number of calving icebergs is increasing due to climate change and, at the same time, the number of ships, especially in the Northern Hemisphere, has tripled in recent decades [12–14]. In particular, the shipping routes in the Arctic region linking the Atlantic and Pacific Oceans are becoming ever more accessible (due to the reduction in sea ice cover), enabling shorter sailing times and leading to reductions in costs and emissions [15]; consequently, Arctic waters are becoming more and more dangerous for shipping due to the risk of ship–iceberg collisions, with an average of around 2–3 incidents per year recorded over the last century [16,17], with numbers continuing to rise.

1.1. State of the Art

In recent years, numerous studies have attempted to monitor and detect icebergs, mainly using three types of platforms: ships, using radar or visual sightings [18]; aircraft, conducting aerial patrols (e.g., International Ice Patrol—IIP) with various types of acquisition systems on board; and satellites, carrying active or passive instruments. The first two are time-consuming, expensive and unable to reach remote locations; for some of the maritime observations, a knowledgeable crew is crucial for the correct interpretation of the instruments (e.g., radar) that may not always automatically detect all responses [19]. Recent developments in satellite technology have revolutionised the way icebergs can be observed and studied, as they can provide high spatial resolution, global coverage and, in many cases, free access to data collected in near real time (e.g., Sentinel constellations from European Space Agency).

Several satellite technologies have been used to monitor icebergs in polar regions. Active instruments such as scatterometers [20], altimeter radars [21,22] and Synthetic Aperture Radar (SAR) have been widely used for iceberg detection [23–34] thanks to their ability to penetrate clouds and also operate at night, mainly using algorithms that are mostly based on the higher radar backscattered signal compared to the surrounding sea. Nevertheless, the IIP itself—which provides iceberg position data also derived from SAR—reports that target classification with these instruments is particularly challenging, especially when compared to the use of optical images [35]. In fact, to create databases on icebergs, the IIP proposed, in some cases, the use of passive instruments as a support for

the active ones starting from 2021. This is because detection using the latter is particularly complex [29,36,37] and, in the context of SAR products, the variability of backscattering intensity, associated with meteorological and oceanic conditions as well as the geometric characteristics of icebergs, requires manual corrections to distinguish the ice blocks from background noise [38].

On the other hand, numerous studies have focused on data acquired by passive optical sensors [39–50], exploiting the spectral response of icebergs in the visible and near-infrared domains, characterised by higher reflectances than the surrounding sea; most of this research is based on a traditional iceberg detection approach, which normally uses fixed threshold techniques.

First Sulak et al. [39], and later Scheick et al. [42], used the panchromatic band in images acquired by Landsat polar platforms to determine the presence of icebergs in their regions of interest, classifying all pixels that exceeded the established reflectance thresholds—0.28 and 0.19, respectively—as "ice blocks". Neuhaus et al. [43], using high-resolution images acquired by the Worldview 1 and 2 satellites, selected a threshold corresponding to the highest pixel value among those belonging to the ocean, and subsequently classified all pixels exhibiting reflectance higher than the identified value as icebergs.

Others, however, have used the near-infrared (NIR) band 8 of data acquired by the Sentinel-2 (S2) constellation. In particular, Moyer et al. [41], with the aim of investigating seasonal variations in the freshwater inflow from icebergs into a Greenlandic fjord, proposed two different reflectance thresholds to be applied to the NIR band, depending on the season in which the icebergs are identified. A lower threshold (0.13) is used for images acquired during summer, and a higher threshold (0.30) for data acquired in the fall, due to differing lighting conditions.

Rezvanbehbahani et al. [44], taking advantage of the data acquired in band 8 of the same constellation, applied a reflectance threshold of 0.13 to the S2 Top Of Atmosphere product (images not atmospherically corrected). They subsequently highlighted how this choice made it difficult to identify icebergs occupying less than 3–4 pixels and how groups of small icebergs were classified as a single large object. Using the same satellite data as in the study just mentioned, Fisser H. [46] employed a different threshold in the Barents Sea region, classifying all pixels with a reflectance in band 8 greater than 0.12 as icebergs. Still, Fisser et al. [47], in a different study, specify that this threshold allows for reliable iceberg detection only under lighting conditions where the Solar Zenith Angle (SZA) is less than or equal to 65°.

Conversely, Heiselberg P. and Heiselberg H. [40], using atmospherically corrected images (the "Level 2A" product) acquired by S2 over Greenland and Denmark, proposed a threshold that works as a primary filter to distinguish sea pixels from all other pixels identifiable as "objects" above it (namely icebergs, ships, ship-wakes and boats). In this case, the threshold was not applied to a single band, but to a more complex index, called I_4, represented by the sum of the reflectance recorded in the four high-resolution bands (visible and NIR), minus the marine background value. It was noted that the minimum threshold required to identify objects changes depending on the conditions of the observed scene; a higher threshold was chosen for detection in the Arctic seas, whereas a lower one was chosen in the case of a normal marine background. In 2020, Heiselberg [45] used the same fixed-threshold methodology proposed in 2017 to identify objects on the sea surface; however, in this case, the index to which the threshold was applied was determined by considering only the red (B4) and NIR bands. Subsequently, various filtering techniques were employed to reduce false alarms caused by land, islands, clouds and waves, excluding, for example, some stationary objects—such as wind turbines—by comparing images acquired in the same location but at different times.

1.2. Background and Related Works

The studies mentioned above, which used optical band data to detect icebergs, suggest that fixed-threshold methodologies are dependent on the observer's judgement. The threshold choice is often subjective and determined through trial and error; thresholds may work well for the single image used for calibration, but there is a chance that errors will occur when applied to different images acquired in the same place but at different times [51]. In fact, different lighting conditions also play a key role, causing changes in surface reflectance depending on the season in which they are observed [52]. Furthermore, fixed-threshold techniques depend on the region of interest and environmental variability, making them specific to a particular area or a specific image dataset, but reducing their effectiveness when the region of interest or weather conditions change [53]. Finally, a threshold determined using images from a specific instrument may not be suitable when applied to data acquired by a different sensor [54].

Some examples help to illustrate the disadvantages mentioned above associated with fixed-threshold methods that are applied to detect icebergs. The first one concerns the methodology proposed by Heiselberg P. and Heiselberg H. in 2017 [40], which used a subset of the image acquired by S2 on 26 September 2016 in the waters surrounding Nuuk, labelling icebergs, or "other objects" (ships, ship-wakes and boats) on the sea surface, all those pixels characterised by reflectance index $I_4 > 500$ (threshold for polar regions), and then categorised them (Figure 1). Using this approach, the authors were able to identify a total of 25 icebergs (of varying sizes), six ship-wakes and five ships/boats. However, in reality the objects n. 4 (identified as a ship-wake), n. 12, n. 42 and n. 43 (identified as ships/boats) in Figure 1 correspond, in the scene under examination, to islands and/or coastlines.

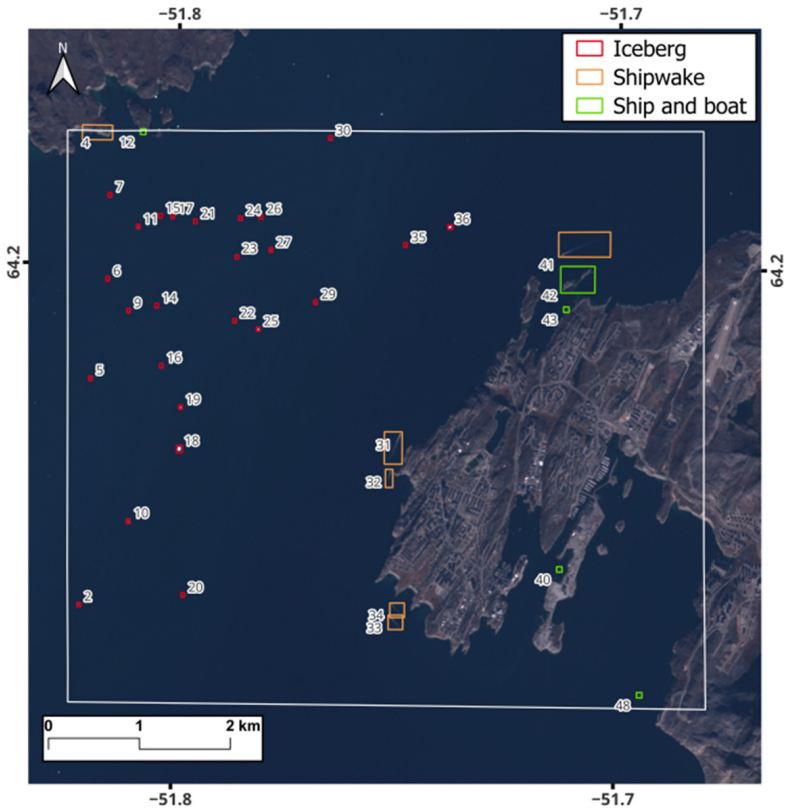


Figure 1. Results by Heiselberg P. and Heiselberg H. [40] over Nuuk (Greenland) based on the S2 (Level 2A) image (tile 22 WDS) collected on 26 September 2016 (RGB in background). Different coloured small boxes represent the different kinds of objects on the sea surface characterised by $I_4 > 500$. The inner white box represents the actually investigated area (adapted from [40]).

Figure 2 shows the results of the same approach applied to a section of the Labrador Sea, observed on 10 August 2021 by the S2 constellation. Heiselberg P. and Heiselberg H.'s methodology was able to identify a good number of icebergs present in the scene, nevertheless also yielding dozens of false positives.

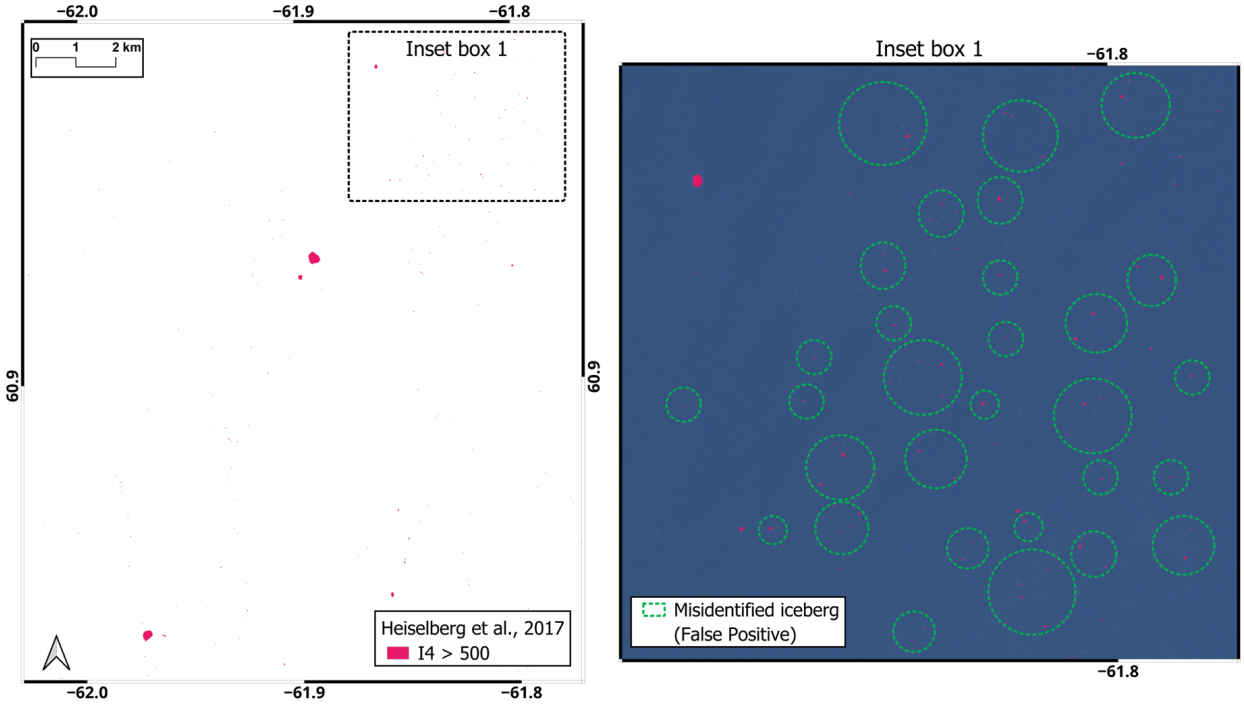


Figure 2. Result of applying the $I_4 > 500$ index [40] to a portion of the Labrador Sea. Image acquired on 10 August 2021 by S2 (Level 2A), tile 20 VNN. Inset box 1 on the right (RGB in background) shows an area within the region of interest where some of the numerous false positives, highlighted by the green dotted circles, have been detected.

Two further fixed-threshold approaches, this time using the NIR band (S2 band 8), were proposed by Moyer et al. [41] and Fisser [46]. The proposed reflectance thresholds were 0.3 for the first methodology and 0.12 for the second one. Compared with Heiselberg P. and Heiselberg H.'s [40] results in Figure 1, the algorithm proposed by Moyer et al. [41] identifies only iceberg n. 18, missing a significant number of ice blocks located in the analysed area (Figure 3). As shown in Figure 4, even when using the Fisser threshold, besides the four icebergs (n. 18, 19, 25 and 36) and two vessels (n. 41 and 31) detected, many others remain undetected. The high number of false negatives (i.e., missed icebergs) observed in both cases is evidently due to the fact that not all ice blocks within the study area exhibit near-infrared reflectance values exceeding the predefined threshold. As previously discussed, these thresholds were derived from specific satellite images acquired in geographical settings that are different from those shown in Figure 1. This finding highlights one of the main limitations of fixed-threshold approaches, whose effectiveness is strongly dependent on the characteristics of the scenario (region, season, etc.) under consideration. Consequently, their application to different areas of interest becomes challenging without prior calibration of the thresholds used, leading to both false positives and false negatives, as shown in Figures 2–4.

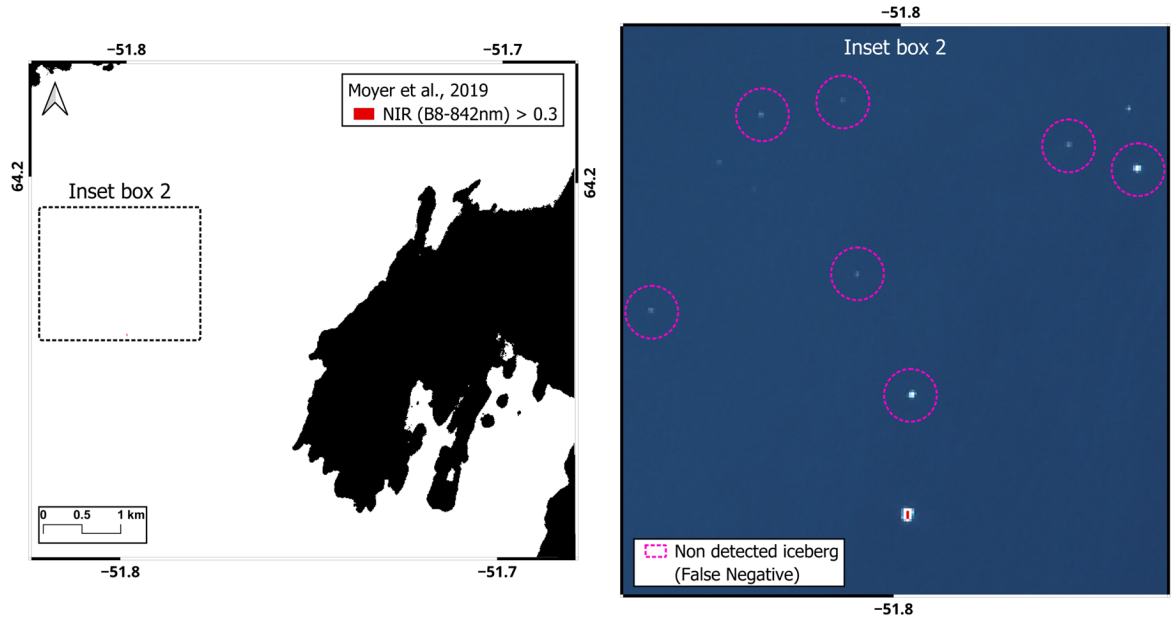


Figure 3. Results of the application of the fixed-threshold algorithm for iceberg detection using NIR band proposed by Moyer et al. [41]. The inset box 2 shows the position of some of the undetected icebergs in the area of interest, circled in bright pink (RGB background). Image Level 1C was acquired on 26 September 2016 by the Sentinel-2 constellation, tile 22 WDS.

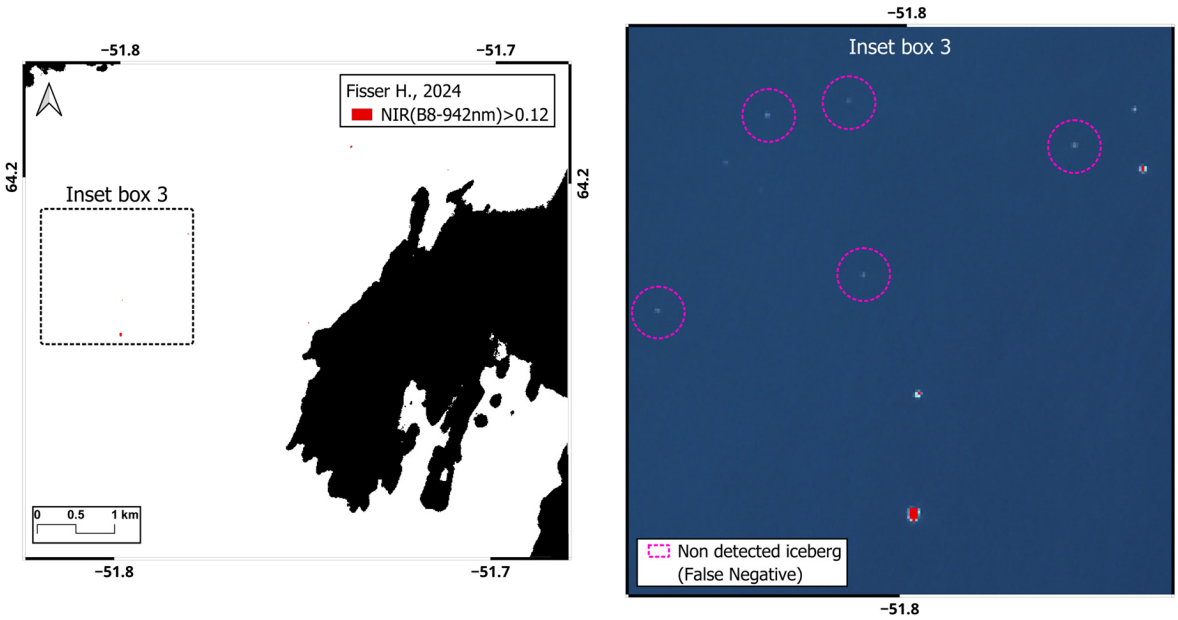


Figure 4. Results of the application of the fixed-threshold algorithm proposed by Fisser [46] for iceberg detection using the NIR band of the S2 image (Level 1C, tile 22 WDS) acquired on 26 September 2016. The inset box enlarged on the right shows, circled in bright pink, some of the undetected icebergs in the area of interest with RGB background.

1.3. The Proposed Approach

To overcome the above-mentioned disadvantages of fixed-threshold methods, a different approach is therefore presented in this paper. The proposed methodology is a robust data analysis technique called Robust Satellite Techniques (RST, [55,56]), a statistical approach initially named RAT (Robust AVHRR Techniques) after its first application to the Advanced Very High Resolution Radiometer (AVHRR) by Tramutoli in 1998 [55]. In recent decades, the proposed methodology has been widely applied for environmental hazard

monitoring and mitigation (e.g., [56]), pipeline network monitoring (e.g., [57]), and near real-time detection of fires (e.g., [58,59]), burned areas (e.g., [60]) and oil spills (e.g., [61,62]). Furthermore, the technique has been utilised for the thermal monitoring of volcanoes (e.g., [63,64]), seismically active areas (e.g., [65–72]), and most recently, forest stress due to climate change (e.g., [73]). Although the general RST framework is well established, the methodological contribution of this study lies in its iceberg-specific implementation based on pixel-wise, multi-temporal reference fields. This unsupervised configuration requires neither labelled training data nor manually calibrated reflectance thresholds. At the application level, this represents the first use of RST for detecting and monitoring icebergs above the sea surface.

By using optical satellite data acquired by the Multispectral Instrument (MSI) on-board the European Space Agency's (ESA) Sentinel-2 constellation, and implementing the methodology using the web-based geospatial analysis platform Google Earth Engine (GEE), two different testing areas were used in this study. The first one is located along the western coast of Greenland, near the Davis Strait and more specifically within a segment of the ocean in the area surrounding the capital city of Nuuk. In addition, a second area of interest (AOI) was identified along the east coast of Canada, in the Labrador Sea, with the purpose of testing the exportability of the considered algorithms.

The work will be organised as follows. Section 2 presents the testing areas, the used data, and the proposed methodology, whilst Sections 3 and 4 set about illustrating and discussing, respectively, the results obtained and future developments in this work. The conclusions of the study are presented in Section 5.

2. Materials and Methods

2.1. Case Studies

The present study focuses on two areas of interest located in the regions already mentioned in Section 1.3, where the analysis was carried out during the months in which the ice is most prone to melting and fragmentation. Additionally, these months offer the advantage of a reduced likelihood of overcast conditions.

2.1.1. Nuuk Region, Greenland

Nuuk, the capital of Greenland, has the largest port in the region and is taking on an increasingly strategic role in trade and tourism routes [74]. Indeed, the city is located in a natural inlet within the Davis Strait, at the entrance to Baffin Bay, which, together with the Northwest Passage, represents an important route connecting the Atlantic and Pacific oceans [75]. Concurrently, a series of tidewater glaciers (e.g., Narsap Sermia) are located to the northeast of Greenland's capital, from which icebergs form and discharge directly into the Nuuk fjord [76]. Driven by currents and wind patterns, these freshwater ice blocks could drift southwards and concentrate in the surrounding waters, thereby posing significant challenges to navigation safety and offshore activities. For this reason, it is particularly important to provide near real-time information on icebergs to ensure safety during navigation. In this regard, nautical charts above 60° north latitudes do not provide comprehensive data regarding icebergs; it is noteworthy that these records are not published with any degree of regularity, and moreover, they merely indicate the prevalence of waters characterised by a high concentration of icebergs [13], often without providing the exact positions of the icebergs themselves.

The first AOI, located in Nuuk and illustrated herein (see Figure 5), covers an area of approximately 232.45 km^2 and is centred at 64.2°N, 51.8°W in the WGS 84 reference system (EPSG:4326).

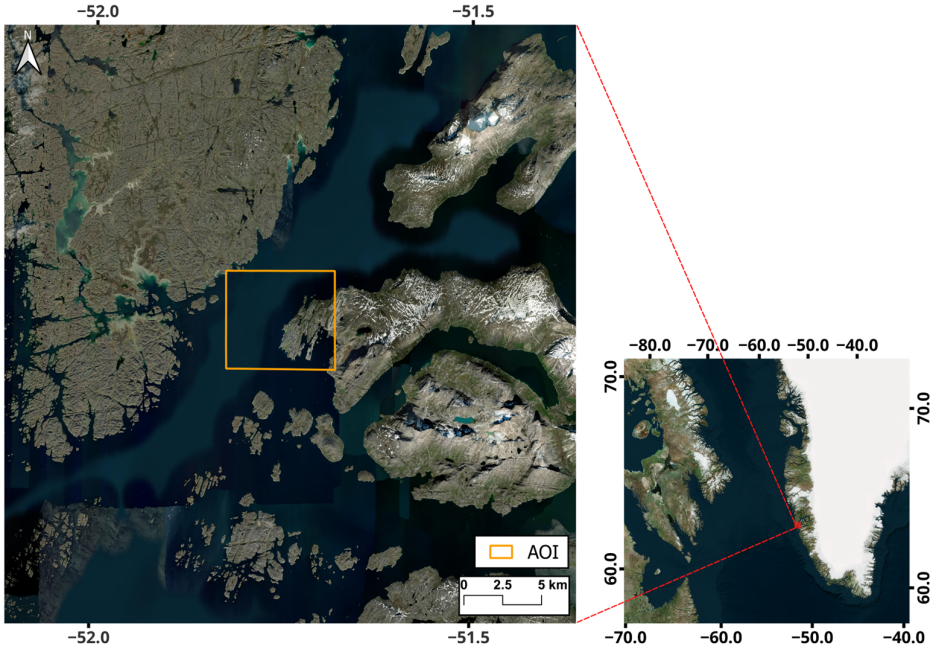


Figure 5. Geographical overview of the area of interest located around the city of Nuuk, Greenland—WGS 84 (EPSG:4326). Image background obtained from Microsoft Bing Maps (© Microsoft Corporation).

The use of the same study area as that employed by Heiselberg P. and Heiselberg H. [40] enabled a comparison with the results achieved by other algorithms regarding the icebergs identified using the same satellite data on the same date.

2.1.2. Newfoundland and Labrador, Canada

Another area significantly affected by drifting icebergs, particularly during the warmer months of the year, is the Labrador Sea, which lies off the eastern coast of Canada and has oceanic and atmospheric circulation patterns that cause ice blocks to drift towards lower latitudes, following the coastline [77–79]. For this reason, the area is of particular interest in terms of monitoring and mapping the icebergs present there, which generally reach this region after breaking away from the ice shelves located along Greenland's western coast [80]. In particular, the stretch of the Labrador Sea that connects to the Hudson Strait has, over the last few decades, proved to be the area with the most significant growth in shipping traffic within the Canadian Arctic, mainly due to new economic and commercial ambitions as well as an increase in tourism [14,81]. The significant change in the configuration of navigable routes originates from the substantial reduction in sea ice concentration, observed mainly along the eastern and northeastern coasts of Canada [82,83].

The second AOI (Figure 6) was identified along the east coast of Canada, in the northernmost part of the Newfoundland and Labrador region, near the Hudson Strait, which represents the entrance to the Northwest Passage. This region, centred at 60.8°N, 62.0°W in the WGS 84 reference system (EPSG:4326), covers an area of 455.71 km^2. In particular, the area is located in the Labrador Sea (approximately 277 km from the coastline), and therefore experiences different weather conditions from Nuuk, which is more sheltered as it is located within a narrow bay.

This weather difference is particularly evident in terms of the intensity of sea surface winds and surface oceanic currents, such as those associated with the Labrador Current System. The latter, which flows in a southeasterly direction along the continental shelf, has its origins in the convergence of the West Greenland Current, the Baffin Island Current, and the waters from the Hudson Strait. The currents within this system have been observed to attain speeds of approximately 0.8–1 m/s [78], thereby facilitating the movement of

icebergs in proximity to Saglek Bank (North Labrador Coast) at velocities approaching 0.52 m/s during the period spanning July and November [84].

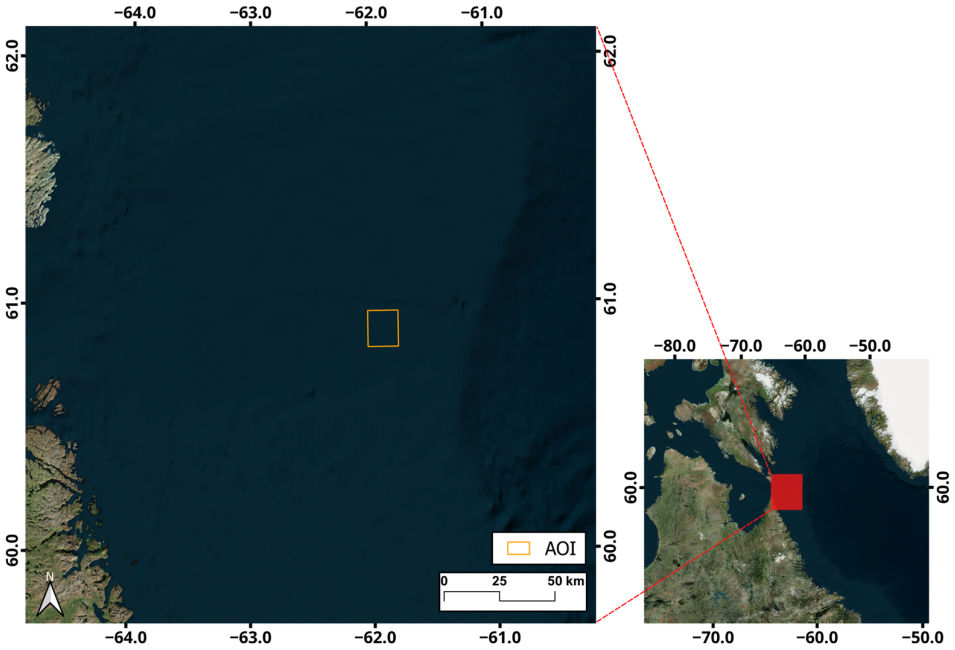


Figure 6. Spatial overview of the section of the Labrador Sea selected as the second area of interest—WGS 84 (EPSG:4326). Image background obtained from Microsoft Bing Maps (© Microsoft Corporation).

It is also worth noting that, following the Titanic disaster in 1912, the IIP initiated a programme of aerial patrols along the entire eastern Canadian coast, with a particular focus on the areas between 40.0° and 52.0°N and between 39.0° and 57.0°W. This mission, which has been ongoing since 1913, is designed to detect icebergs in the North Atlantic Ocean and issue warnings to mariners operating in these waters [85]. This organisation provides annual datasets (in CSV format since 2002) containing information on the positions of icebergs, integrating data acquired through aerial surveys with data obtained from ship sightings, satellite surveys and buoys. In particular, analysis of the 2021 database identified a region in the northern Labrador Sea where both Sentinel-2 imagery and iceberg sighting data from the IIP were available for the same period. These concurrent data sources enabled assessment of the accuracy and sensitivity of the iceberg detection methodology proposed in this study within this area of interest.

2.2. Input Data and Tools

This study is based on the analysis of data acquired by MSI onboard the ESA's Sentinel-2 constellation, which provides high spatial resolution observations from the visible up to the short-wave infrared at resolutions from 10 m to 60 m. A key advantage of the S2 mission for this application is its high revisit frequency at polar latitudes; in fact, while the nominal revisit time is five days at the equator, it significantly increases towards higher latitudes, reaching intervals shorter than two days. With the recent addition of Sentinel-2C, the temporal sampling is further improved, allowing more than 16 acquisitions over a 20-day period in Arctic regions [86], making the constellation particularly suitable for monitoring more dynamic phenomena such as drifting icebergs. Therefore, in the present article, satellite sensors that are generally utilised for the study of slow dynamics at high spatial resolution are used, also benefitting from a high temporal resolution.

Iceberg detection was performed using Level-1C (L1C) Top Of Atmosphere (TOA) reflectance data, focusing on the green band (B3, 560 nm) at 10 m spatial resolution. This

band was selected due to the strong radiometric contrast between icebergs and the surrounding seawater, with ice exhibiting significantly higher reflectance values in the visible domain. A multi-temporal dataset, namely "Harmonized Sentinel-2 MSI: MultiSpectral Instrument, Level-1C (TOA)", spanning the period 2016–2025 was processed within the GEE environment, which enables efficient access to large satellite archives and supports automated analysis workflows [87,88].

2.3. Methodology

As discussed briefly above, the methodology used in this study is known as RST, a statistical approach based on multi-temporal analysis of satellite data [55,56]. By examining the behaviour of the data in unperturbed conditions, this change-detection method enables the identification of statistically significant (at various confidence levels) anomalous signals, without the requirement for preliminary assumptions or auxiliary data. Consequently, it can be identically applied to different geographical areas and satellite data. It is devoted to automatically discriminating anomalous signal transients from signal variations related to observation conditions or normal variability of the signal itself, by calculating the Absolutely Llocal Index of Change of the Environment (ALICE, where the use of the double "*l*" was introduced by Tramutoli (1998) [55] to refer to a specific time t and location (x,y) in the space/time domain), as illustrated in Equation (1):

$$\otimes(x,y,t) = \frac{V(x,y,t) - \mu_V(x,y)}{\sigma_V(x,y)} \quad (1)$$

with $V(x,y,t)$ representing the value of the signal V, measured at the point with coordinates (x,y) and at time t, whilst $\mu_V(x, y)$ and $\sigma_V(x, y)$, are the temporal mean and the standard deviation of the signal, respectively. These, hereinafter referred to as "reference fields", represent the unperturbed conditions of the signal under examination and are determined from a multi-year data set derived from cloud-free satellite imagery, representative of the most homogeneous acquisition conditions, both in the spatial domain (same geographical area) and in the temporal domain (same month, same time of day). In particular, the parameter $\mu_V(x, y)$, calculated at the pixel level within the given interval, represents the expected value in the absence of disturbances, whilst $\sigma_V(x, y)$ provides an estimate of the normal variability of the signal $V(x,y,t)$ itself. Reference field computation is carried out using a Kσ-clipping procedure (for details see [55] and references therein) to remove outliers from the time series.

Reduced noise is associated with the normal variability of the signal. In this context, noise refers to the ordinary, non-anomalous variability of the satellite signal arising from spatial effects (e.g., orography), temporal patterns (e.g., daily/annual cycles) and changing of observational conditions (e.g., solar illumination, satellite view angle). By automatically accounting for these site-specific effects, the method is intrinsically robust against the proliferation of false alarms and mostly unaffected by the limitations associated with the fixed-threshold methods mentioned above. In addition, the ⊗ index is a standardised variable that weights the difference between the measured signal and the expected signal, and the historical variability of the signal within the same pixel. Therefore, higher absolute values of the index correspond to increasingly significant statistical deviations. In fact, assuming the ALICE index to be a quasi-Gaussian variable characterised by a mean of zero and a standard deviation of one [64,89], absolute values greater than 2σ have a probability of occurrence of less than 5 per cent, decreasing rapidly to less than 0.3 per cent for values exceeding 3σ.

To perform iceberg detection, this work uses the signal measured in band B3 of Sentinel-2/MSI (S2-MSI) images as variable $V(x,y,t)$ in Equation (1). Two distinct datasets of co-

located, temporally homogeneous (between 14:59–15:13 UTC for Nuuk and 15:35–15:40 for Labrador) images acquired across the 10-year period 2016–2025 were collected to compute corresponding reference fields, $\mu_{B3}(x, y)$ and $\sigma_{B3}(x, y)$, for each test area. Specifically, one dataset comprises 114 September images for the Nuuk case study, while the other includes 104 August observations for the Newfoundland and Labrador region. Neither dataset includes the images analysed during the change detection phase, i.e., 26 September 2016 for Nuuk case and 10 August 2021 for the Labrador Sea region. An iterative asymmetric Kσ-clipping was applied to remove outliers associated with objects exhibiting high reflectance values in the B3 band such as clouds, marine vehicles and icebergs; k = 2 was selected since, in a Gaussian distribution, ±2 sigma includes approximately 95 per cent of the natural fluctuations of the signal. To remove cloudy pixels from MSI-S2 Level 1C (TOA) images, a cloudy mask was created using the "Sentinel-2: Cloud Probability" (S2-CP) dataset, which provides, at 10 m spatial resolution, the probability that each pixel is affected by cloud cover. In particular, a join was performed between the S2-CP and the S2 image collection used (filtered on the basis of their respective areas of interest and the period analysed, with reflectance values scaled and divided by 10,000 so as to yield values between 0 and 1) in order to add a further band to the images in the collection, containing information about the probable cloud cover for each pixel in every single image. Following this, a function was developed to ensure that all pixels with a probability of cloud cover of 30 per cent or more were excluded from the calculation of the reference fields.

For the Nuuk case study, a land–sea mask was additionally used. While any standard static land–sea mask could serve this purpose, a dynamic approach was adopted to generate a tailored mask best suited to the target image. Specifically, the mask was generated from a long-term Sentinel-2 median composite calculated using only May-to-August acquisitions to avoid the presence of any sea ice or snow. The Normalised Difference Water Index (NDWI) was thus calculated on the median composite [90]. Pixels with NDWI $\geq$ 0.4 [91,92]—a conservative threshold determined through a process of trial and error—were subsequently labelled as sea, whereas all remaining pixels were classified as land and excluded from subsequent calculations. After these pre-processing operations, an additional condition was introduced in order to ensure a sufficiently large dataset; for each location (x, y), more than 15 useful (i.e., not cloudy, not outlier) observations were required. Therefore, all pixels with 15 or fewer useful observations were excluded from the ALICE index calculation. The following table (Table 1) contains relevant information about the data used to perform change detection in the two areas of interest.

Table 1. Summary of the data used to apply the RST methodology in the two areas of interest.

AOI	Sensor Information	Acquisition Date for Change Detection	Analysed Image ID	Tot. Images Used for Reference Fields
Nuuk (64.2°N, 51.8°W) ext. 232.45 km^2	B3 band S2-MSI Tile 22WDS	26 September 2016 15:09 UTC	COPERNICUS/S2_HARMONIZED/20160926T150952_20160926T150955_T22WDS	114
Labrador (60.8°N, 62.0°W) ext. 455.71 km^2	B3 band S2-MSI Tile 20VNN	10 August 2021 15:39 UTC	COPERNICUS/S2_HARMONIZED/20210810T153911_20210810T153908_T20VNN	104

Following application of the RST methodology, the resulting outputs were validated, wherever possible, against the database provided by the IIP. Where ground-truth data were unavailable—as is often the case in iceberg detection owing to the rapid spatio-temporal variability of iceberg shapes, sizes and locations—the results were assessed through visual inspection, a practice widely adopted in this field [30–32,40,42,50]. This visual assessment

was further supported by transept-based plots showing the spatial distribution of B3 reflectance across each candidate iceberg (see the Supplementary Materials).

3. Results

3.1. Case Study—Nuuk, Greenland

The application of the aforementioned $\otimes_{B3}$ criterion (Equation (1)) was based on the spectral behaviour of icebergs, with the results presented in Figure 7. It has been observed that the pixels belonging to the ice blocks exhibit remarkably elevated ALICE index values (up to 109 when observing only the highest anomalies), which highlights reflectance values that are clearly anomalous compared to those expected (multi-temporal mean) on sea pixels.

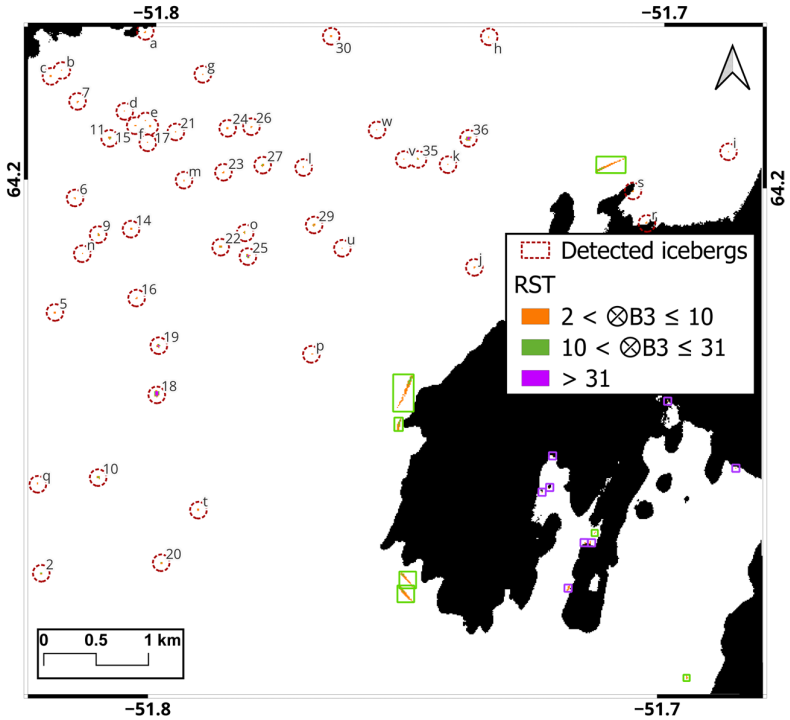


Figure 7. Application of $\otimes_{B3}$ index on the 26 September 2016 at 15:09 (UTC) S2 image in the Nuuk AOI; the result shows $\otimes_{B3} > 2$ based on three different colour patterns; the mainland is shown in black, using the land–sea mask. The red dotted circles indicate the identified icebergs (labelled with numbers and letters), the green rectangles indicate the boats, and the purple ones highlight the "other objects".

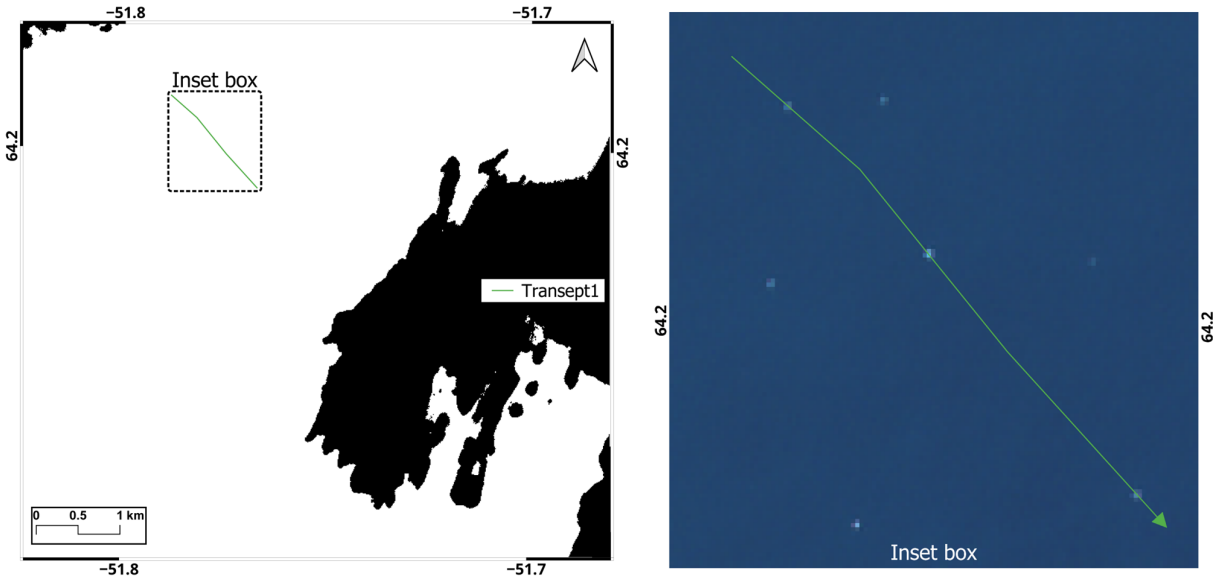
By comparison with the information on the icebergs present in the same scene, as reported by Heiselberg P. and Heiselberg H. [40] in Figure 1, it should be noted that at values of $\otimes_{B3} > 2$, a larger number of icebergs was identified. In total, 63 objects were identified in the scene: 48 icebergs (the 25 identified in Heiselberg P. and Heiselberg H.'s study, plus 23 additional "candidate icebergs"), seven boats (the same classified as "ships" in the Heiselbergs study), and eight "other objects", mainly located along the coast and within the city's port area. These objects are associated with temporary mobile platforms (whose position may vary slightly over time) and reefs sometimes emerging from the sea surface. As expected, no false positives resulted, unlike in the case of Heiselberg P. and Heiselberg H.'s study, in association with permanent land pixels. It is important to emphasise at this point that, using the fixed threshold proposed by Moyer [41], it would have been possible to identify just one iceberg among those present in the AOI around Nuuk, whereas with Fisser's [46] threshold, the number would have increased only slightly, making it possible to detect just four icebergs.

The following table (Table 2) summarises the data presented in Figure 7 and provides additional insights into the number of anomalous pixels identified at $\otimes_{B3} > 2$. The relative area occupied by these pixels is also delineated, along with the objects identified on the sea surface.

Table 2. Summary of objects (corresponding to pixels with $\otimes_{B3} > 2$) detected within the Nuuk AOI.

RST-Objects in Nuuk AOI			
Alice Index $\otimes_{B3}$	**Number of Pixels**	**Area (m^2)**	**Identified Objects**
$\otimes_{B3} > 2$	431	43,100	48 icebergs; 7 moored and sailing ships; 8 other objects

As shown below, to better illustrate the potential advantages of using the RST approach over fixed-threshold techniques for iceberg detection, a transept was drawn across a portion of the image under investigation. Figure 8 shows the location and orientation of "Transept1" within the Nuuk AOI, intersecting three small icebergs (with a horizontal extent at sea level ranging from 15 to 60 m; [93]) also identified in the study by Heiselberg P. and Heiselberg H. [40] in the same area (namely icebergs 24, 27 and 29 in Figure 1).



(**a**) (**b**)

Figure 8. (**a**) Geographical location of "Transept1" (shown in green), which crosses a section of the MSI-S2 image acquired in the Nuuk AOI on 26 September 2016. (**b**) A detailed view of the box depicted on the left: the green transept intersects three small icebergs in the area (RGB background).

Based on the transept described above, the results obtained using the RST methodology were compared with those derived from the two fixed-threshold approaches applied to NIR S2 band 8 (B8) and proposed by Moyer [41] and Fisser [46]. It is worth recalling the discussion presented in the Introduction (Section 1): namely, that a reflectance threshold of 0.3 was adopted for the AOI in Nuuk in Moyer's approach because the satellite image was acquired in autumn, whereas a threshold of 0.12 was used in Fisser's approach.

Figure 9a illustrates the spatial variation in the signal and shows that, when the two fixed-threshold methods are applied, pixels 14, 51 and 107—which belong to the three icebergs—are not classified as ice because their reflectance values in Band 8 (NIR) fall below the adopted thresholds, resulting in false negatives. By contrast, the same three pixels are correctly identified as icebergs by the RST approach, as their reflectance values in Band

3 are classified as anomalous, with $\otimes_{B3}$ index values exceeding two, as indicated by the arrows in Figure 9b.

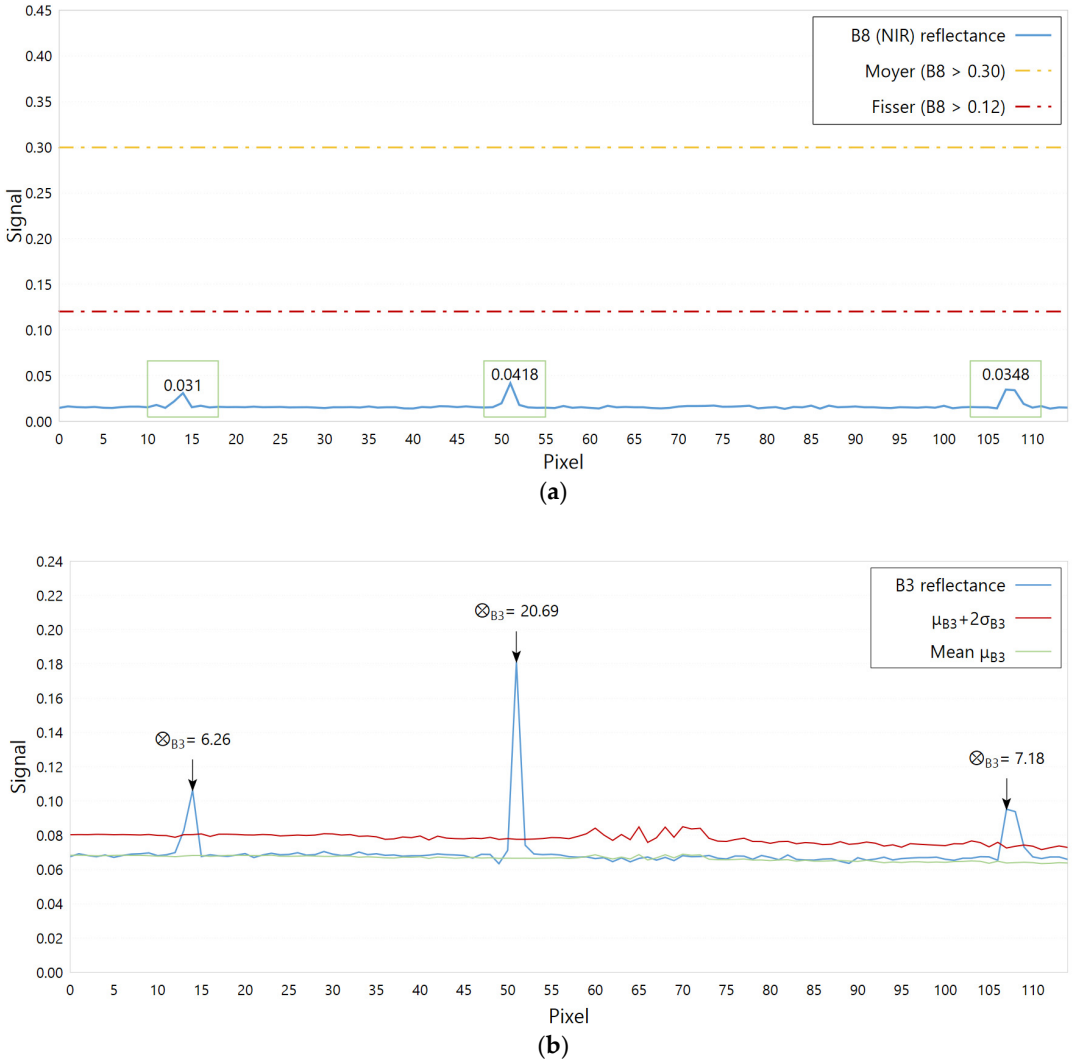


Figure 9. The graphs show the signal trend along transept 1; (**a**) shows the spatial distribution of reflectance in band 8 (NIR) along "Transept1" within the image acquired by S2, as well as the corresponding thresholds proposed by Moyer [41] and Fisser [46]. Green-bordered squares indicate the pixels (nos. 14, 51 and 107) where false negatives occur. Graph (**b**) highlights the spatial trend of the parameters used by the RST approach for the identification of anomalous pixels. In this case, anomalies are detected at pixels 14, 51 and 107.

3.2. Additional Case Study—Newfoundland and Labrador Region, Canada

As described in Section 2 ("Materials and Methods"), an additional test was carried out in a sector of the Labrador Sea, off the northeastern coast of Canada, in order to evaluate the performance of the considered iceberg detection method in different environmental and seasonal conditions.

For the Labrador Sea AOI, the information provided by the IIP, whose 2021 database indicates the presence of five large icebergs on the selected date and area of interest, was considered for validation. Figure 10 shows the results obtained using the RST approach: 13 icebergs are identified already at $\otimes_{B3} > 10$, with $\otimes_{B3}$ values generally higher than 30 (reaching up to 107 at a pixel belonging to iceberg n. V). This means, higher and higher reliability, as higher and higher values of the Alice index, corresponds to more and more rare events.

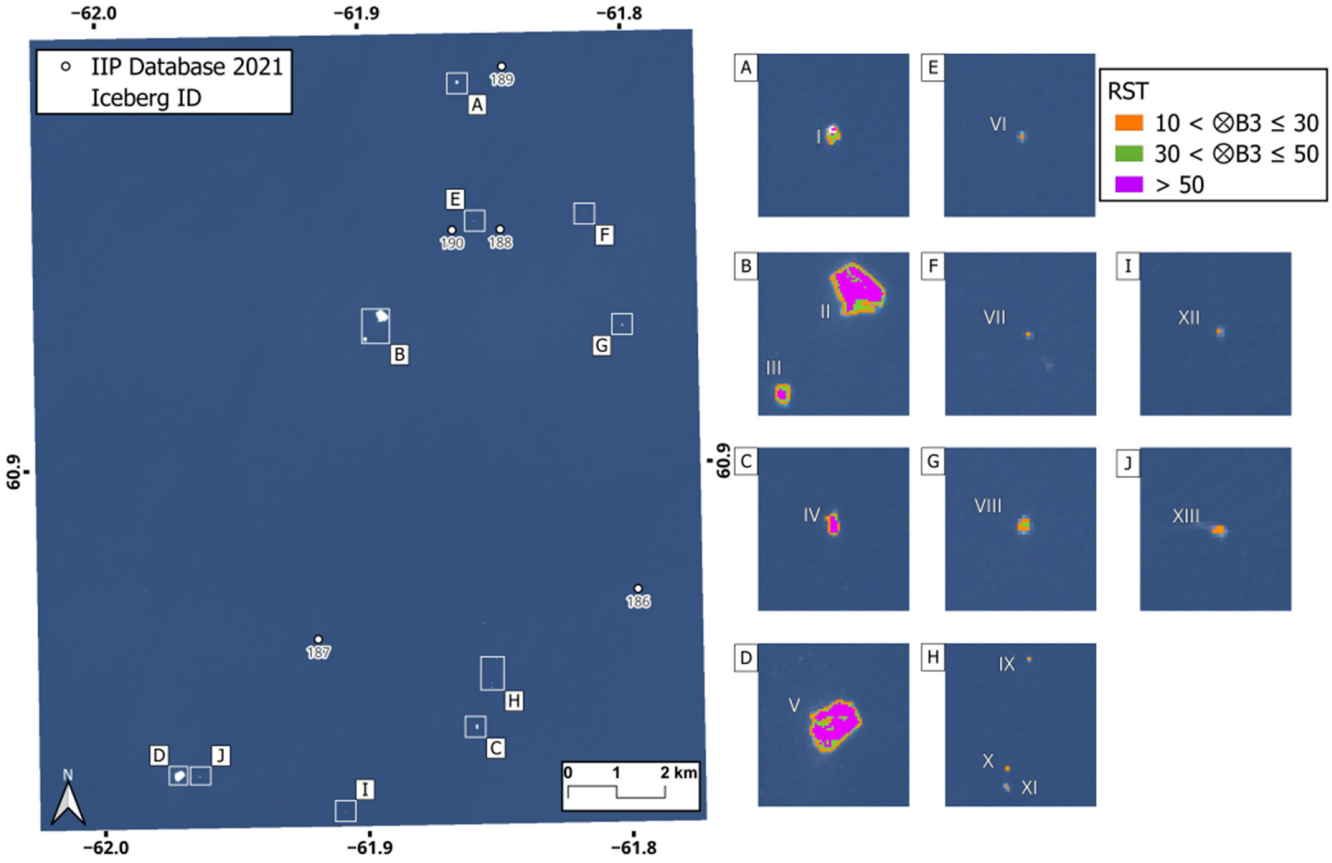


Figure 10. Application of the RST approach to the S2 image of 10 August 2021 at 15:39 (UTC) within the Labrador Sea (RGB in background). The spatial distributions of $\otimes_{B3}$ values around the icebergs identified at $\otimes_{B3} > 10$ are displayed in the insets on the right (**A**–**J**), together with their RST identifier numbers (I to XIII).

Among them:

- The ones numbered from I to V correspond to the five icebergs reported by the IIP. As can be seen in Figure 11, the positions of the icebergs identified in the image utilised for change detection do not coincide exactly with those indicated in the IIP database due to the time difference between the sighting time recorded by the IIP and the time at which the Sentinel-2A platform passed the area. In fact, the first case involves a radar/visual sighting by the Canadian Coast Guard (CGBT) at 08:52 UTC, while the satellite image was acquired approximately six and a half hours later, at 15:39 UTC, on the same day. During this time, the five icebergs may have been carried southwest by the Labrador Sea's cold currents, which typically move from north to south along Canada's east coast [78], winds and waves. The distances traversed by the icebergs examined, all along the same direction (southwest), ranging from 1.89 km to 8.83 km approximately (see Figure 11), are in fact in line with Dalton's conclusions in 2025 [3], who stated in his study that icebergs can reach top speeds of up to 2.3 m/s.
- The ones numbered from VI to XIII correspond to eight potential additional ice blocks detected, with wide widths ranging from 10/20 to 70 metres, for a total of 167 anomalous pixels. Therefore, these smaller additional "candidate icebergs" appear to fall into the category between "Bergy Bits", which have widths between 5 and 14 metres, and "Medium Bergs", which range from 61 to 122 metres [93].

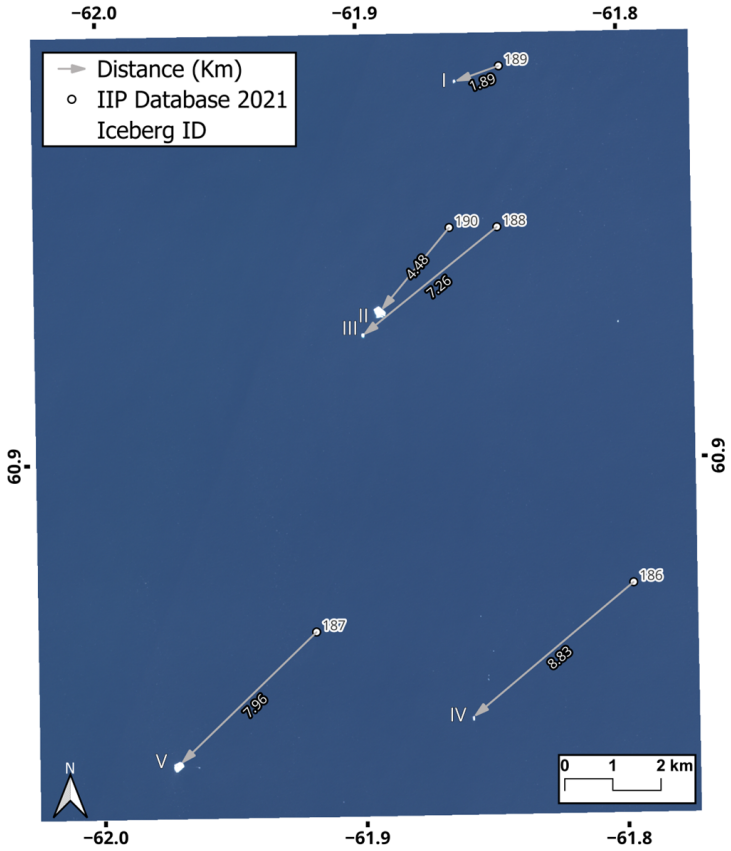


Figure 11. Distance between the positions of the five icebergs recorded in the IIP database, sighted at 08:52 UTC on 10 August 2021 in the Labrador Sea AOI, and the ones (numbered from I to V) detected by RST within the image acquired by S2 on the same day at 15:39 UTC (RGB background).

Comparing these results, once again, with the ones of the fixed-threshold methodologies discussed earlier, it is important to note that:

- By using the I_4 index proposed by Heiselberg P. and Heiselberg H. [40], it would have been possible to identify the five icebergs recorded by the IIP, but at the same time, this would have resulted in dozens of false positives, as shown in Figure 2 in the introduction;
- By applying the thresholds proposed by Moyer [41] and Fisser [46]—which in this case are almost identical, as the image analysed was acquired in August (meaning that Moyer's threshold changes from 0.3 to 0.13, whilst Fisser's remains at 0.12)—it would be possible to identify all the icebergs present in the IIP dataset, and just one of the small icebergs not recorded by the organisation operating along the Canadian coast, bringing the total to six;
- The RST methodology, applied to the B3 band, enabled the identification of the largest number of icebergs (13) present in the area under investigation, while at the same time avoiding false positives.

For this second case study, two further transepts, "Transept 2" and "Transept 3", were drawn across the S2 image of the Labrador Sea collected on 10 August 2021. The location of "Transect 2" is shown in Figure 12. In Figure 13, the values of the I_4 index—computed following Heiselberg P. and Heiselberg H. [40]—across "Transept2" are depicted.

The graph in Figures 13 and 14 shows that, by applying both the Heiselberg P. and Heiselberg H. [40] fixed-threshold method and the RST approach, the iceberg reported as n. 186 by the IIP is correctly detected at pixels 190,192–194 along the transept.

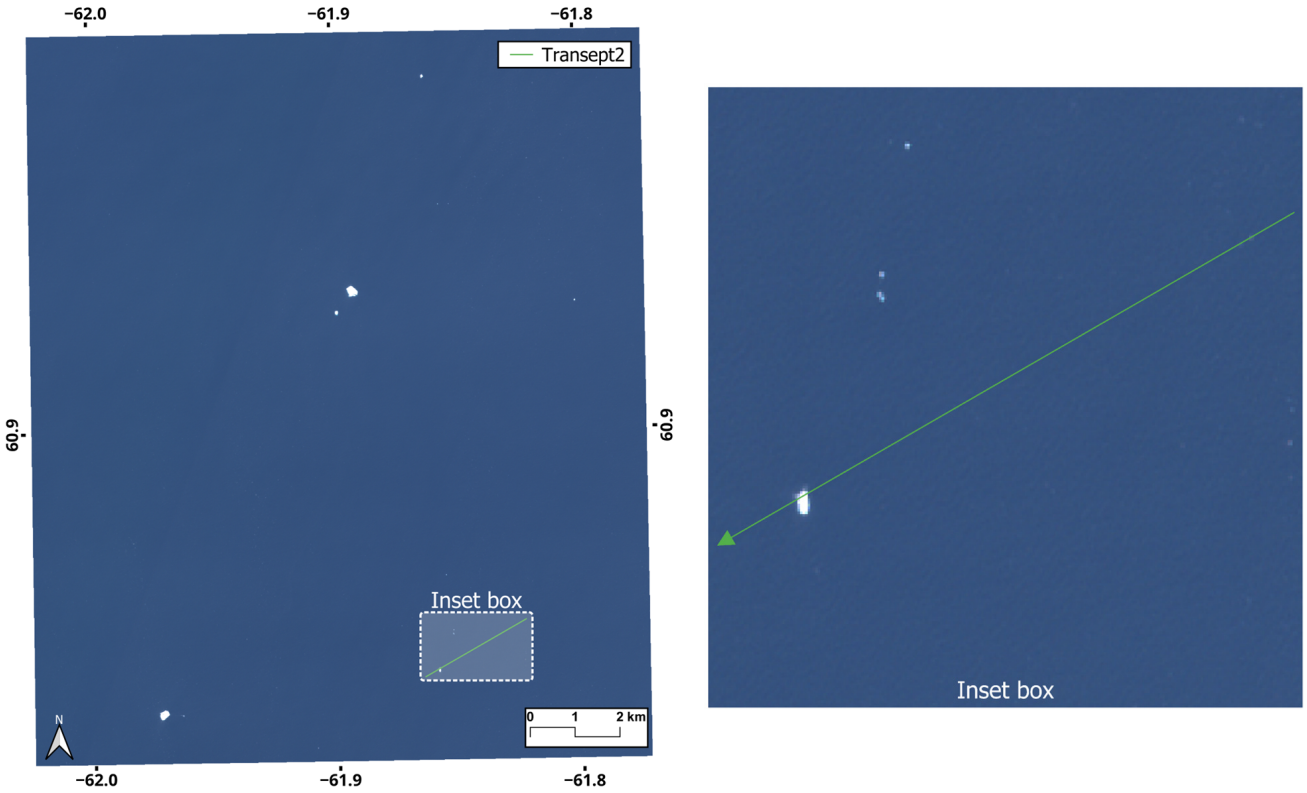


Figure 12. MSI-S2 image acquired in the Labrador Sea AOI on 10 August 2021 (RGB in background): (**a**) geographical location of "Transept2" (dashed white box) and (**b**) close-up view of the green transept that intersects the iceberg (IIP n. 186, RST id n. IV).

However, in Figure 13, around pixel 18 (highlighted by the black-bordered box), over-threshold I_4 values seem to indicate the presence of an object on the sea surface which apparently does not exist. In fact, fixed-threshold methods can be prone to false positives related to the natural variability of the sea surface that, in particular conditions (e.g., sea roughness caused by adverse weather, sun-glint phenomenon, bathymetry changes due to tidal cycles) can reach over-threshold values even in the absence of any superficial object.

The same does not happen when the RST approach (Figure 14) is applied. In fact, around pixel 18, over-threshold $\otimes_{B3}$ values are not reached thanks to the higher value of $\sigma_{B3}(x,y)$—typically associated with locations/periods characterised by high signal variability—that, in Equation (1), prevents $\otimes_{B3}(x,y,t)$ from reaching higher and higher values as far as the values of the denominator $\sigma_{B3}(x,y)$. For this reason, false positives can be avoided by RST, even in the presence of high B3 reflectance measured in particular sea surface conditions.

On a further transept—"Transept3", plotted within the same image in Figure 15—the performance of the other two fixed-threshold methods (Figure 16) proposed by Moyer et al. [41] and by Fisser [46], as well as the ones achieved by the RST approach (Figure 17), were analysed.

From an inspection of Figures 16 and 17, it can be concluded that:

- All considered methods appear capable of detecting the largest iceberg at the bottom of the inset in Figure 15b, corresponding to the iceberg reported as n. 186 by the IIP and also included in the previous "Transept2". It is detected by RST (applied to B3 reflectances), at pixels from 142 to 149 along "Transept3" and at pixels from 144 to 148, by using the Moyer and Fisser thresholds applied to NIR band 8 (B8). The apparent minor extension of the iceberg detected using the B8 band is not surprising

considering the higher penetration in the sea water of B3 radiation (compared with the B8 one) [94–97] which allows us to receive the reflected signal even from the submerged part of the iceberg itself.

- In addition, along the upper section of "Transept3", three further objects can be easily recognised on the sea surface (Figure 15b) as further small "candidate icebergs" not included in the IIP dataset. Regarding these three objects, from Figure 16 it is evident that both the two fixed-threshold approaches may have resulted in false negatives, i.e., missed icebergs. On the contrary (arrows in Figure 17), they are detected at pixels 5, 55–56 and 63, by RST (with quite significant $\otimes_{B3}$ values from 11 up to more than 16) as the icebergs n. IX, X and XI of Figure 10.

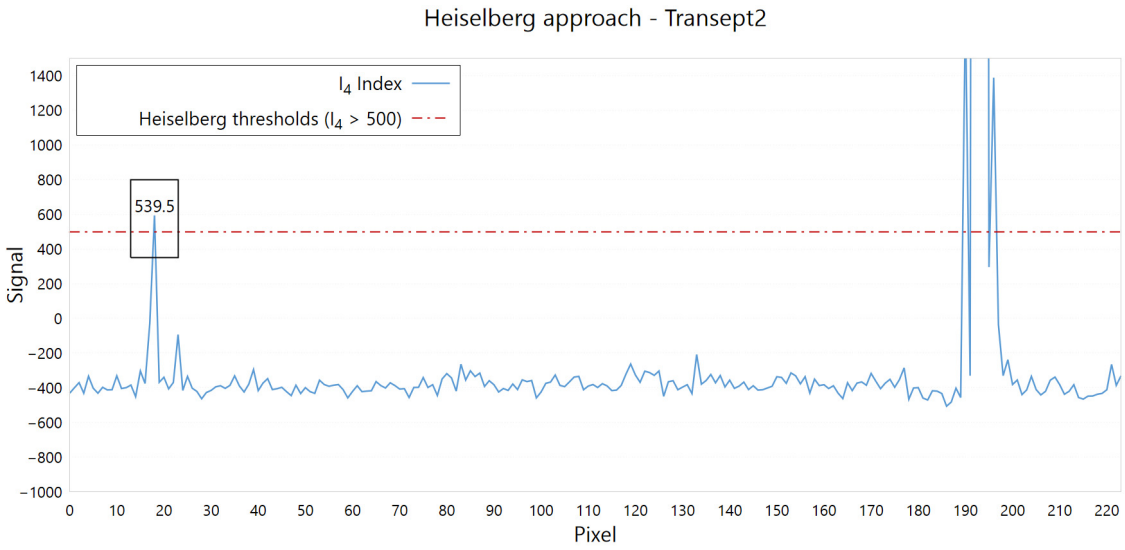


Figure 13. The plot shows the spatial distribution of the I_4 index proposed by Heiselberg P. and Heiselberg H. [40] along "Transept2"; the black-bordered square indicates the pixel (no. 18) where a false positive occurs.

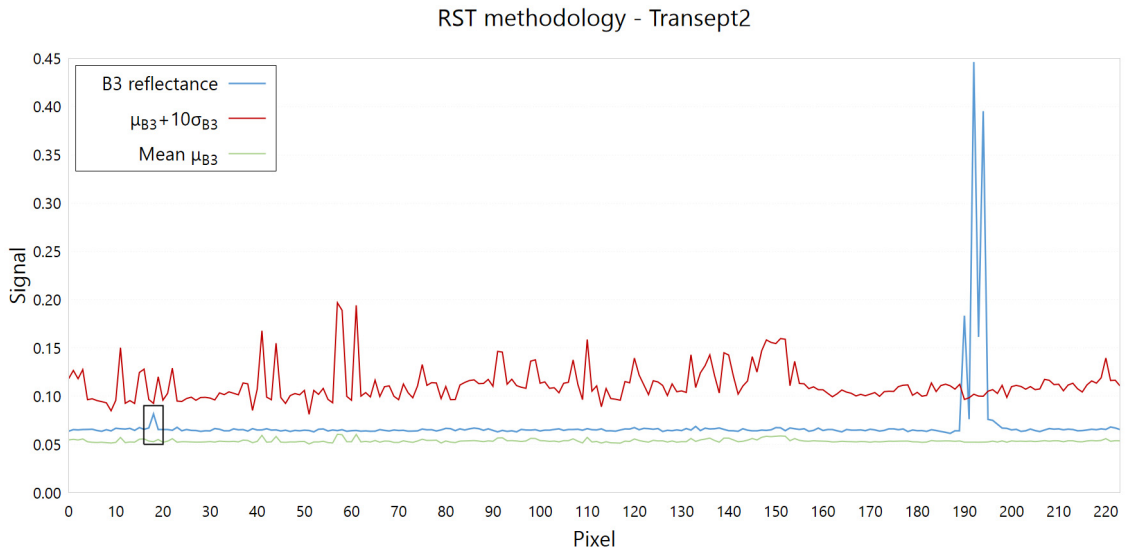


Figure 14. The graph highlights the spatial distribution, along the "Transept2" of the parameters used in the RST methodology to identify anomalous values associated with icebergs. The black-bordered square indicates the pixel no. 18 with no associated anomalies. Note that the large iceberg reported as n. 186 by the IIP is correctly identified by RST (as. n. IV) at pixels 190, 192–194, with $\otimes_{B3}$ values well above 10 (from 20 up to 70).

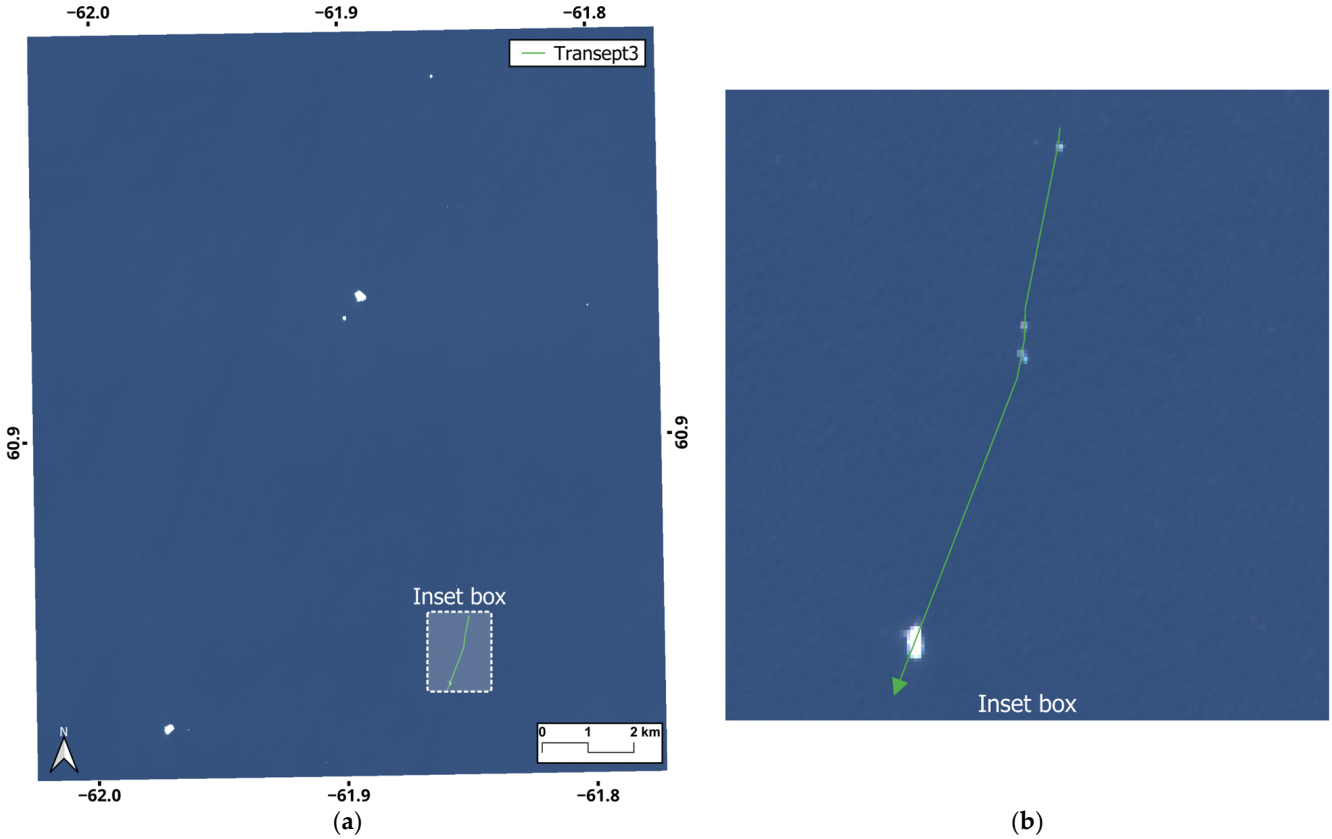


Figure 15. MSI-S2 image acquired in the Labrador Sea AOI on 10 August 2021 (RGB in background): (**a**) geographical location of "Transept3" (dashed white box) and (**b**) a detailed view of the area of the dashed white box depicted on the left: the green line ("Transept3") intersects four icebergs in the area.

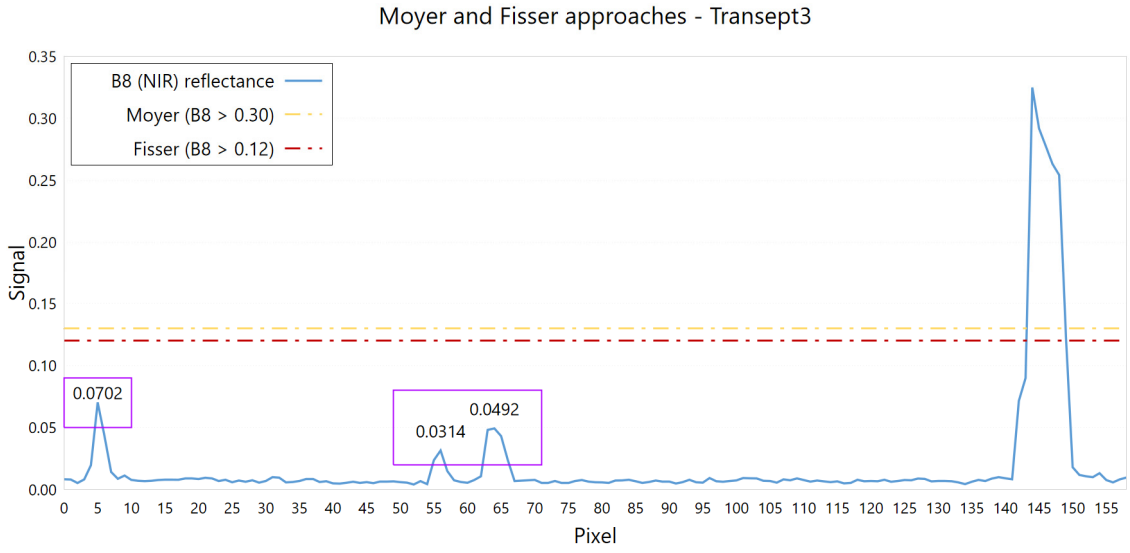


Figure 16. Spatial distribution along "Transept3" of reflectance values in the NIR band (B8 of S2) and the corresponding thresholds set by Moyer [41] and Fisser [46] for iceberg detection. The purple boxes highlight the pixels corresponding to the three "candidate icebergs" not identified by the two fixed threshold methods.

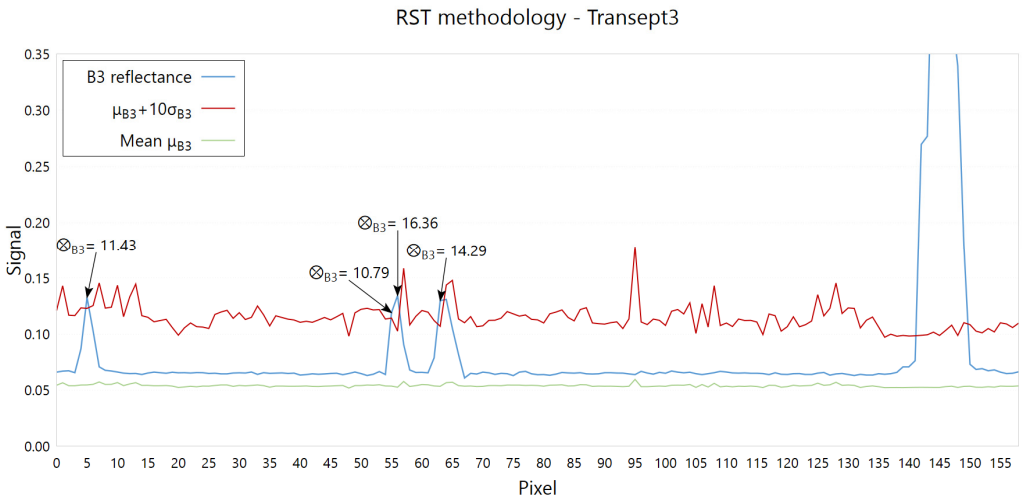


Figure 17. Spatial distribution along "Transept3" of reflectance values in the VIS band (B3 of S2) and related parameters used by the RST-based iceberg detection. The arrows highlight the pixels (with $\otimes_{B3} > 10$) identified as "candidate icebergs," also reporting the associated $\otimes_{B3}$ value.

4. Discussion

The early detection of drifting icebergs is crucial for navigation safety and offshore activities, as it helps to prevent accidents and, at the same time, allows for the monitoring of their evolution in space and time, providing the opportunity to take precautions or corrective action. In order to provide timely information, a constellation of polar satellites was selected. In fact, satellite observations from polar-orbiting constellations are particularly suitable for monitoring high latitudes where they can achieve much shorter revisit times, enabling daily monitoring of large oceanic areas.

The present study provides an initial validation of this iceberg-specific RST configuration. The RST methodology is applied for the first time to the visible band B3 of S2-MSI for the timely and automatic detection of icebergs in the polar regions. Its intrinsic and easy exportability to different geographic areas, periods, and sensors represents one of the main advantages of the proposed approach, which will allow the results of the preliminary tests presented in this study to be extended to a more extensive data set. In the present study, and in comparison with traditional fixed-threshold methods, RST demonstrated a higher sensitivity (in detecting even very small icebergs) with a negligible number of false positives (about zero if all the other objects representing a danger for navigation are considered).

False positives were particularly considered in the Nuuk test-case, where not just icebergs but also other kinds of objects that are potentially dangerous for navigation [98–100], such as vessels and shallow features (e.g., reefs) emerging near the coastline, were detected by RST. Vessel movements are generally monitored through the Automatic Identification System (AIS); however, in polar regions some ships may transmit weak or unreliable signals due to technical limitations or environmental conditions. In other situations, AIS transmitters may be deliberately switched off in order to avoid geolocation, a practice often associated with so-called "shadow fleets" [101]. In both cases, vessels may remain undetected by conventional monitoring systems and therefore represent potential hazards for navigation that are comparable to drifting icebergs. Additionally, the obligation to communicate via AIS is not applicable to small vessels and military ships [45]. For these reasons, it is frequently challenging to obtain frequent and up-to-date information about icebergs and ships at high latitudes. In this context, satellite-based anomaly detection may also contribute to the identification of surface objects that could otherwise remain unnoticed. Anomalies associated with reefs or shallow waters were identified exclusively

near the coast and, specifically, within the port area, where vessels typically operate with greater caution and at limited speeds. RST methodology, applied to the B3 band, allows the identification of a large number of potential icebergs, even at the expense of including other surface objects such as vessels or shallow features; however, this is useful for safe navigation purposes.

Conversely, the analysis conducted in the Labrador Sea regards a scenario that is different from the one previously analysed, with no shallow waters or vessels. In a less disturbed context, icebergs were detected at very high relative intensities (from $\otimes_{B3} > 10$ up to $\otimes_{B3} > 107$ on the icebergs also reported by the IIP), allowing the detection of even very small ice objects (not listed in the IIP database) with high confidence and zero false positives.

The RST methodology was successfully applied to the detection of icebergs by using a single S2 spectral band (B3), and the findings demonstrate that results achieved in this way are comparable or better than those achieved, on the same data, by prior research employing fixed-threshold approaches to one S2 band, or even more.

Compared with their first application, when applied to different geographic areas, all the considered fixed-threshold methods were the worst performing, showing a proliferation of false positives and/or of missed detections.

A further salient aspect pertains to the method's capacity to deliver, with a non-supervised classification, results in a timely manner thanks to the shorter revisiting time of polar-orbiting satellites at high latitudes and to the large volume of open-access ESA data available within the GEE environment. When suitable satellite acquisitions are available, this may represent a significant advantage compared to traditional in situ reconnaissance activities (e.g., aerial and naval surveys) carried out by the IIP along the Canadian east coast, which are both time-consuming and costly. Moreover, even when the IIP uses data from satellite constellations equipped with radar instruments (e.g., ESA Sentinel-1, RADARSAT Constellation Mission) to detect icebergs, this does not guarantee that the results of the identification process will be available within a short timeframe. Indeed, the data from the previous 24 h must first be downloaded by analysts, who must then process it manually, one by one, to verify which objects are actually icebergs and which are not [35]. This highlights the value of having an intrinsically exportable methodology such as RST (e.g., [55,56,58,102,103]), which, together with a tool such as GEE, could enable straightforward, efficient and timely investigations on icebergs on a global scale in any geographical area, at any time and by using different sensors. This would facilitate analysis in remote and large areas in which obtaining data through in situ investigations would be particularly complex or, in some cases, impossible.

Limitations and Future Developments

Despite the promising results, it is important to take into account some limitations associated with the optical iceberg detection in the Arctic marine environment, such as the frequent cloud cover, which can prevent observation of the sea surface [104].

In addition, multispectral instruments operating in the Solar Reflectance spectral region require daylight conditions and, at high latitudes, during the winter months, low solar elevation angles (SZA $\approx 90°$) limit the availability of the reflectance data. Regarding the RST approach, one of the main challenges is managing the large size of the dataset required for its application. In this study, a minimum of 15 images for the same month over the reference period (e.g., 2016–2025) was considered sufficient to obtain quite stable $\mu(x,y)$ and $\sigma(x,y)$ reference fields. However, larger datasets (~80 images) have been suggested (e.g., [105]) to ensure their actual stability.

Discussing the results obtained by the method in the context of the existing challenges of detection in marine areas near the Arctic, although RST reduces false alarms associated with the normal spatial and temporal variability of the sea surface, further validation is also needed in the presence of sea ice or brash ice and under highly variable sea states or strong sun-glint conditions.

In relation to the above limitations, future developments of this study—with further analyses to be carried out in other geographical contexts—include the integration of the iceberg monitoring system with image datasets provided by other optical satellite sensors, whilst also considering applying the RST methodology to other spectral bands, and in particular:

1. The ones operating on the Landsat 8 and Landsat 9 satellite platforms (launched in February 2013 and September 2021, respectively). Both platforms are equipped with an Operational Land Imager (OLI), a multispectral sensor operating in the visible and NIR at 30 m, and a Thermal Infrared Sensor (TIRS), which acquires thermal infrared (TIR) data at 100 m (resampled to 30 m to match OLI data). At latitudes above 60°, Landsat satellites provide images with a revisit time well below 8 days (frequency at the equator), achieving up to 85 per cent swath overlap at the highest latitudes [106]. Their Mean Local Solar Time (MLST) value is very close to the overflight time of the S2 constellation satellites (10:00 a.m. ±15 min for Landsat 8/9, 10:30 a.m. for S2). This temporal compatibility may facilitate the integration of multispectral datasets acquired from the two constellations, enabling the acquisition of a greater number of consecutive images in the optical band this way, increasing the possibility of cloud-free observations as well as monitoring continuity. Moreover, the RST strategy could be extended to TIR sensors like LANDSAT/TIRS (e.g., [61]), leveraging the complementary value of jointly exploiting optical and thermal information [107] to also detect icebergs during the polar nights. Again, the higher temporal repetition guaranteed for polar satellite sensors in polar regions makes possible what will be very complicated to achieve at lower latitudes (mostly because of the insufficient number of images available for reference field computation).
2. The Visible Infrared Imaging Radiometer Suite (VIIRS), flying on board the Suomi National Polar-orbiting Partnership (NPP) and NOAA-20 and -21 platforms. It has an extremely sensitive panchromatic band, known as the Day/Night Band (DNB), which spans from the visible spectrum (0.5 μm) to the near-infrared (0.9 μm) and is capable of collecting spectral data both during the day and at night, even under very low light conditions [108,109]. In fact, it is capable of utilising not only sunlight but also sources such as light from the moon, the aurora borealis and atmospheric glow, making it a useful tool for collecting information both at night and during those periods of the year (late November to early January) when the sun is very low on the horizon in the polar regions. Using the constellation of three VIIRS satellite sensors, it would be possible to obtain, at latitudes greater than 55°, more than eight images per day with a native spatial resolution of approximately 375 metres [108]. Such extraordinary VIIRS-DNB capabilities, together with the enhanced sensitivity guaranteed by the RST approach, could compensate for the loss of signal intensity associated with the lower spatial resolution compared with both the S2 and LANDSAT sensors, and could, for example, enable the detection and tracking of large bergs even in the absence of sunlight.

5. Conclusions

Despite considerable advances in the field of sensors and remote sensing techniques, iceberg detection remains a particularly complex and challenging task. Icebergs represent a

significant hazard, particularly in the context of navigation safety and offshore activities. In this study, the RST methodology was employed for the first time to identify icebergs, using Sentinel-2 optical data acquired by the MSI sensor and, specifically, using only the B3 band centred at 560 nm.

Regarding detection performance, in the Nuuk test case, the RST approach identified all the icebergs reported by Heiselberg P. and Heiselberg H. [40], together with additional "candidate icebergs" and other objects on the sea surface, without generating false positives related to permanent land pixels. It should be noted that the non-iceberg objects (e.g., ships and reefs) identified by RST correspond to information that is usually already available to navigators who can easily distinguish them from icebergs. However, such information remains valuable, particularly at high latitudes where some vessels may not reliably transmit their position through the AIS, thereby posing a potential risk to surrounding maritime traffic. Conversely, the other two considered fixed-threshold methods that showed, in this case study, very poor iceberg detection capabilities, missing almost all the icebergs present in the area.

The analysis performed on the second testing area along the northeastern coast of Labrador allowed us to test and compare the exportability of the iceberg detection methodologies in different geographical and seasonal contexts. The RST method, applied to the B3 band, confirmed its detection capability, successfully identifying all the icebergs reported by IPP, as well as additional smaller "candidate icebergs", without false positives. By contrast, the fixed-threshold methods either missed several icebergs or produced a very high number of false positives.

It should be emphasised that the RST approach is intrinsically and easily exportable on different geographic areas, temporal periods and sensors, as widely demonstrated in many other studies in which the methodology has been used. In fact, being solely based on the satellite data at hand, the only requirement for its implementation is the availability of a sufficiently long time series of satellite imagery collected in observational conditions similar to the image at hand. As also shown in this study, no assumption and no adjustment are required when moving from one test case to another, from one sensor to another.

We have seen in this study how much the high temporal resolution of the S2 constellation at polar latitudes, in conjunction with the implementation of the RST methodology within the GEE environment, facilitated and accelerated the automation of the iceberg detection process, also opening to further practical implications. For instance, as a future development, the possibility of implementing an automated plugin within the GEE environment can be explored, which would be capable of providing maritime operators with systematic updates on iceberg (and additional potentially dangerous objects) presence along the main shipping routes in the Arctic regions.

Notwithstanding some limitations related to cloud cover and illumination conditions and the need to perform further analyses in more complex environments (e.g., in the presence of sea ice), the proposed approach provides a simple and scalable framework for iceberg monitoring, offering a great trade-off between detection reliability and sensitivity. Its applicability to different regions and the potential integration with additional satellite datasets further support its use for large-scale and operational iceberg detection, especially when considering the busiest Arctic shipping routes.

Supplementary Materials: The following supporting information can be downloaded at https://www.mdpi.com/article/10.3390/rs18203526/s1. An additional file contains details about the spectral reflectance profile in the Sentinel-2 B3 band (green at 560 nm, with a spatial resolution of 10 m) for those objects identified in the text as 'candidate icebergs'.

Author Contributions: Conceptualisation, I.M. and V.T.; methodology, I.M. and V.T.; software, I.M., R.C. and N.G.; validation, I.M., R.C. and C.F.; formal analysis, I.M. and M.L.; resources, I.M. and C.F.; data curation, I.M.; writing—original draft preparation, I.M.; writing—review and editing, I.M., V.T. and R.C.; visualisation, I.M.; supervision, V.T. All authors have read and agreed to the published version of the manuscript.

Funding: This work was supported by the European Union—NextGenerationEU under the Italian National Recovery and Resilience Plan (NRRP), Mission 4, Component 2, Investment 3.3 (D.M. 630/2024)—PhD Program in Engineering for Innovation and Sustainable Development (Ingegneria per l'Innovazione e lo Sviluppo Sostenibile) at the University of Basilicata (Università degli Studi della Basilicata), CUP: C37G24000280006.

Data Availability Statement: Data used to implement RST for iceberg detection within the Google Earth Engine platform are available in the Earth Engine public catalogue and can be found here: https://developers.google.com/earth-engine/datasets/catalog/COPERNICUS_S2_HARMONIZED (accessed on 30 June 2026); https://developers.google.com/earth-engine/datasets/catalog/COPERNICUS_S2_CLOUD_PROBABILITY (accessed on 30 June 2026). The IIP's iceberg dataset is available here: https://nsidc.org/data/g00807/versions/1#anchor-data-access-tools (accessed on 30 June 2026).

Conflicts of Interest: The authors declare no conflicts of interest.

Abbreviations

The following abbreviations are used in this manuscript:

IIP	International Ice Patrol
SAR	Synthetic Aperture Radar
NIR	Near-infrared
SZA	Solar Zenith Angle
S2	Sentinel-2
MSI	Multispectral Imager
RST	Robust Satellite Techniques
RAT	Robust AVHRR Techniques
ESA	European Space Agency
AOI	Area of Interest
GEE	Google Earth Engine
S2-MSI	Sentinel-2/MSI
L1C	Level-1C
TOA	Top Of Atmosphere
S2-CP	Sentinel-2: Cloud Probability
ALICE	Absolutely Llocal Index of Change of the Environment
NDWI	Normalised Difference Water Index
S2A	Sentinel-2A
CGBT	Canadian Coast Guard
AIS	Automatic Identification System
OLI	Operational Land Imager
TIRS	Thermal Infrared Sensor
TIR	Thermal Infrared
MLST	Mean Local Solar Time
VIIRS	Visible Infrared Imaging Radiometer Suite
NPP	Suomi National Polar-orbiting Partnership
DNB	Day/Night Band

References

1. Thompson, L.G. Climate Change: The Evidence and Our Options. *Behav. Anal.* **2010**, *33*, 153–170. [CrossRef]

2. Amani, M.; Mehravar, S.; Asiyabi, R.M.; Moghimi, A.; Ghorbanian, A.; Ahmadi, S.A.; Ebrahimy, H.; Moghaddam, S.H.A.; Naboureh, A.; Ranjgar, B.; et al. Ocean Remote Sensing Techniques and Applications: A Review (Part II). *Water* **2022**, *14*, 3401. [CrossRef]
3. Dalton, A.; Garbo, A.; Copland, L.; Van Wychen, W.; Mueller, D.; Tivy, A.; Marson, J.M. Long-Term Field Tracking of Icebergs in the Eastern Canadian Arctic. *Arct. Sci.* **2025**, *11*, 1–22. [CrossRef]
4. Wilson, K.-J.; Turney, C.S.; Fogwill, C.J.; Blair, E. The Impact of the Giant Iceberg B09B on Population Size and Breeding Success of Adélie Penguins in Commonwealth Bay, Antarctica. *Antarct. Sci.* **2016**, *28*, 187–193. [CrossRef]
5. Duprat, L.P.; Bigg, G.R.; Wilton, D.J. Enhanced Southern Ocean Marine Productivity Due to Fertilization by Giant Icebergs. *Nat. Geosci.* **2016**, *9*, 219–221; Correction in *Nat. Geosci.* **2016**, *9*, 728. [CrossRef]
6. Cenedese, C.; Straneo, F. Icebergs Melting. *Annu. Rev. Fluid Mech.* **2023**, *55*, 377–402. [CrossRef]
7. Marsh, R.; Ivchenko, V.; Skliris, N.; Alderson, S.; Bigg, G.R.; Madec, G.; Blaker, A.T.; Aksenov, Y.; Sinha, B.; Coward, A.C.; et al. NEMO–ICB (v1. 0): Interactive Icebergs in the NEMO Ocean Model Globally Configured at Eddy-Permitting Resolution. *Geosci. Model Dev.* **2015**, *8*, 1547–1562. [CrossRef]
8. Merino, N.; Le Sommer, J.; Durand, G.; Jourdain, N.C.; Madec, G.; Mathiot, P.; Tournadre, J. Antarctic Icebergs Melt over the Southern Ocean: Climatology and Impact on Sea Ice. *Ocean Model.* **2016**, *104*, 99–110. [CrossRef]
9. Bigg, G.R. *Icebergs: Their Science and Links to Global Change*; Cambridge University Press: Cambridge, UK, 2015.
10. Akbari, V.; Brekke, C. Iceberg Detection in Open and Ice-Infested Waters Using C-Band Polarimetric Synthetic Aperture Radar. *IEEE Trans. Geosci. Remote Sens.* **2018**, *56*, 407–421. [CrossRef]
11. Ferdous, M.S.; McGuire, P.; Power, D.; Johnson, T.; Collins, M. A Comparison of Numerically Modelled Iceberg Backscatter Signatures with Sentinel-1 C-Band Synthetic Aperture Radar Acquisitions. *Can. J. Remote Sens.* **2018**, *44*, 232–242. [CrossRef]
12. Berkman, P.A.; Fiske, G.J.; Lorenzini, D.; Young, O.R.; Pletnikoff, K.; Grebmeier, J.M.; Fernandez, L.M.; Divine, L.M.; Causey, D.; Kapsar, K.E.; et al. *Satellite Record of Pan-Arctic Maritime Ship Traffic*; NOAA Technical Report OAR ARC 22-10; NOAA: Silver Spring, MD, USA, 2022. [CrossRef]
13. Dalton, A.; Copland, L.; Van Wychen, W.; Dawson, J.; Cook, A.; Garbo, A.; Mueller, D.; Tivy, A. Understanding Changes in Iceberg–Ship Coexistence throughout the Eastern Canadian Arctic: 2012–2019. *FACETS* **2025**, *10*, 1–16. [CrossRef]
14. Halliday, W.D.; Dawson, J.; Yurkowski, D.J.; Doniol-Valcroze, T.; Ferguson, S.H.; Gjerdrum, C.; Hussey, N.E.; Kochanowicz, Z.; Mallory, M.L.; Marcoux, M.; et al. Vessel Risks to Marine Wildlife in the Tallurutiup Imanga National Marine Conservation Area and the Eastern Entrance to the Northwest Passage. *Environ. Sci. Policy* **2022**, *127*, 181–195. [CrossRef]
15. Sibul, G.; Schütz, P.; Fagerholt, K. Arctic Route Planning under Ice Uncertainty: A Risk-Averse Stochastic Shortest Path Problem. *Transp. Res. Part E Logist. Transp. Rev.* **2026**, *205*, 104507. [CrossRef]
16. Hill, B.T. Ship Collision with Iceberg Database. In Proceedings of the SNAME 7th International Conference and Exhibition on Performance of Ships and Structures in Ice, Banff, AB, Canada, 16–19 July 2006.
17. Lee, T.-K.; Park, H.-J. Review of Ice Characteristics in Ship-Iceberg Collisions. *J. Ocean Eng. Technol.* **2021**, *35*, 369–381. [CrossRef]
18. Orheim, O.; Giles, A.B.; Moholdt, G.; Jacka, T.H.J.; Bjørdal, A. Antarctic Iceberg Distribution Revealed through Three Decades of Systematic Ship-Based Observations in the SCAR International Iceberg Database. *J. Glaciol.* **2023**, *69*, 551–565. [CrossRef]
19. Reid, T.; Walter, T.; Enge, P.; Fowler, A. Crowdsourcing Arctic Navigation Using Multispectral Ice Classification & GNSS. In Proceedings of the 27th International Technical Meeting of the Satellite Division of The Institute of Navigation (ION GNSS+ 2014), Tampa, FL, USA, 8–12 September 2014; pp. 707–721.
20. Budge, J.S.; Long, D.G. A Comprehensive Database for Antarctic Iceberg Tracking Using Scatterometer Data. *IEEE J. Sel. Top. Appl. Earth Obs. Remote Sens.* **2018**, *11*, 434–442. [CrossRef]
21. Tournadre, J.; Whitmer, K.; Girard-Ardhuin, F. Iceberg Detection in Open Water by Altimeter Waveform Analysis. *J. Geophys. Res. Oceans* **2008**, *113*. [CrossRef]
22. Braakmann-Folgmann, A.; Shepherd, A.; Ridout, A. Tracking Changes in the Area, Thickness, and Volume of the Thwaites Tabular Iceberg "B30" Using Satellite Altimetry and Imagery. *Cryosphere* **2021**, *15*, 3861–3876. [CrossRef]
23. Howell, C.; Power, D.; Lynch, M.; Dodge, K.; Bobby, P.; Randell, C.; Vachon, P.; Staples, G. Dual Polarization Detection of Ships and Icebergs-Recent Results with ENVISAT ASAR and Data Simulations of RADARSAT-2. In *Proceedings of the IGARSS 2008-2008 IEEE International Geoscience and Remote Sensing Symposium*; IEEE: New York, NY, USA, 2008; Volume 3, pp. III-206–III-209.
24. Wesche, C.; Dierking, W. Iceberg Signatures and Detection in SAR Images in Two Test Regions of the Weddell Sea, Antarctica. *J. Glaciol.* **2012**, *58*, 325–339. [CrossRef]
25. Mazur, A.; Wåhlin, A.K.; Krężel, A. An Object-Based SAR Image Iceberg Detection Algorithm Applied to the Amundsen Sea. *Remote Sens. Environ.* **2017**, *189*, 67–83. [CrossRef]
26. Zakharov, I.; Power, D.; Howell, M.; Warren, S. Improved Detection of Icebergs in Sea Ice with RADARSAT-2 Polarimetric Data. In *Proceedings of the 2017 IEEE International Geoscience and Remote Sensing Symposium (IGARSS)*; IEEE: New York, NY, USA, 2017; pp. 2294–2297.

27. Barbat, M.M.; Rackow, T.; Hellmer, H.H.; Wesche, C.; Mata, M.M. Three Years of Near-Coastal Antarctic Iceberg Distribution from a Machine Learning Approach Applied to SAR Imagery. *J. Geophys. Res. Oceans* **2019**, *124*, 6658–6672. [CrossRef]
28. Koo, Y.; Xie, H.; Ackley, S.F.; Mestas-Nuñez, A.M.; Macdonald, G.J.; Hyun, C.-U. Semi-Automated Tracking of Iceberg B43 Using Sentinel-1 SAR Images via Google Earth Engine. *Cryosphere* **2021**, *15*, 4727–4744. [CrossRef]
29. Færch, L.; Dierking, W.; Hughes, N.; Doulgeris, A.P. A Comparison of Constant False Alarm Rate Object Detection Algorithms for Iceberg Identification in L- and C-Band SAR Imagery of the Labrador Sea. *Cryosphere* **2023**, *17*, 5335–5355. [CrossRef]
30. Færch, L.; Dierking, W.; Hughes, N.; Doulgeris, A.P. Mapping Icebergs in Sea Ice: An Analysis of Seasonal SAR Backscatter at C- and L-Band. *Remote Sens. Environ.* **2024**, *304*, 114074. [CrossRef]
31. Færch, L.; Dierking, W.; Hughes, N.; Doulgeris, A.P. Detecting Arctic Icebergs in Sea Ice in L-Band SAR Images Using a Multiscale CFAR Algorithm. *IEEE J. Sel. Top. Appl. Earth Obs. Remote Sens.* **2025**, *18*, 11867–11876. [CrossRef]
32. Bailey, J.; Stott, J. Feasibility of Deep Learning-Based Iceberg Detection in Land-Fast Arctic Sea Ice Using YOLOv8 and SAR Imagery. *Remote Sens.* **2025**, *17*, 3998. [CrossRef]
33. Wang, C.; Li, X.-M.; Shi, L.; Li, H.; Mouche, A.; Chapron, B. Sentinel-1 Wave Mode SAR Monitoring of Icebergs around Antarctica. *Remote Sens. Environ.* **2026**, *332*, 115094. [CrossRef]
34. Channa, S.; Gadekar, P. An Enhanced Machine Learning Framework for Robust Iceberg Detection in SAR Imagery. In *Proceedings of the 2026 International Conference on Intelligent and Sustainable Electronics & Computing Technologies (INSECT)*; IEEE: New York, NY, USA, 2026; pp. 1–6.
35. International Ice Patrol. *Report of the International Ice Patrol in the North Atlantic—2025 Season*; U.S. Department of Homeland Security—United States Coast Guard: Washington, DC, USA, 2025; p. 90.
36. Rudnickas, D.; Hicks, M.; Hamel, A.; Hirschberg, M. *International Ice Patrol 2021 Annual Report*; Report number: CG-188-76; U.S. Department of Homeland Security—United States Coast Guard: Washington, DC, USA, 2021. [CrossRef]
37. Fisser, H.; Doulgeris, A.P.; Dierking, W. Backscatter-Sensitive Retrieval of Iceberg Areas from Sentinel-1 Extra Wide Swath SAR Data. *Remote Sens. Environ.* **2025**, *331*, 115042. [CrossRef]
38. Barbat, M.M.; Rackow, T.; Wesche, C.; Hellmer, H.H.; Mata, M.M. Automated Iceberg Tracking with a Machine Learning Approach Applied to SAR Imagery: A Weddell Sea Case Study. *ISPRS J. Photogramm. Remote Sens.* **2021**, *172*, 189–206. [CrossRef]
39. Sulak, D.J.; Sutherland, D.A.; Enderlin, E.M.; Stearns, L.A.; Hamilton, G.S. Iceberg Properties and Distributions in Three Greenlandic Fjords Using Satellite Imagery. *Ann. Glaciol.* **2017**, *58*, 92–106. [CrossRef]
40. Heiselberg, P.; Heiselberg, H. Ship-Iceberg Discrimination in Sentinel-2 Multispectral Imagery by Supervised Classification. *Remote Sens.* **2017**, *9*, 1156. [CrossRef]
41. Moyer, A.N.; Sutherland, D.A.; Nienow, P.W.; Sole, A.J. Seasonal Variations in Iceberg Freshwater Flux in Sermilik Fjord, Southeast Greenland from Sentinel-2 Imagery. *Geophys. Res. Lett.* **2019**, *46*, 8903–8912. [CrossRef]
42. Scheick, J.; Enderlin, E.M.; Hamilton, G. Semi-Automated Open Water Iceberg Detection from Landsat Applied to Disko Bay, West Greenland. *J. Glaciol.* **2019**, *65*, 468–480. [CrossRef]
43. Neuhaus, S.U.; Tulaczyk, S.M.; Branecky Begeman, C. Spatiotemporal Distributions of Icebergs in a Temperate Fjord: Columbia Fjord, Alaska. *Cryosphere* **2019**, *13*, 1785–1799. [CrossRef]
44. Rezvanbehbahani, S.; Stearns, L.A.; Keramati, R.; Shankar, S.; Van Der Veen, C.J. Significant Contribution of Small Icebergs to the Freshwater Budget in Greenland Fjords. *Commun. Earth Environ.* **2020**, *1*, 31. [CrossRef]
45. Heiselberg, H. Ship-Iceberg Classification in SAR and Multispectral Satellite Images with Neural Networks. *Remote Sens.* **2020**, *12*, 2353. [CrossRef]
46. Fisser, H. Iceberg Drift Trajectories from Optical Satellite Data in the Barents Sea. In *Proceedings of the 27th IAHR International Symposium on Ice, Gdańsk, Poland, 9–13 June 2024*; Kolerski, T., Ed.; Gdańsk University of Technology Publishing House: Gdańsk, Poland, 2024; Volume 3, pp. 146–158. [CrossRef]
47. Fisser, H.; Doulgeris, A.P.; Høyland, K.V. Impact of Varying Solar Angles on Arctic Iceberg Area Retrieval from Sentinel-2 near-Infrared Data. *Ann. Glaciol.* **2024**, *65*, e38. [CrossRef]
48. Suo, Z.; Lu, Y.; Liu, J.; Ding, J.; Wang, Q.; Li, L.; Ju, W.; Li, M. Extracting Iceberg Freeboard Using Shadow Length in High-Resolution Optical Images. *Geo-Spat. Inf. Sci.* **2024**, *27*, 892–901. [CrossRef]
49. Zhou, Z.; Li, O.; Ai, S.; Chu, X.; Ali Shah, S. Antarctic Iceberg Freeboard Retrieval via Deep Learning from Optical Satellite Imagery. *Int. J. Digit. Earth* **2025**, *18*, 2548005. [CrossRef]
50. Skourup, H.; Buus-Hinkler, J.; Fenger-Nielsen, R.; Soare, G.-V.; Simonsen, S.B.; Rasmussen, T.A.S. Linking Iceberg Detection and Ice-Sheet Discharge: A Case Study in Upernavik Isfjord, Northwest Greenland. *J. Glaciol.* **2026**, *72*, e70. [CrossRef]
51. Reis, L.G.D.M.; Souza, W.D.O.; Ribeiro Neto, A.; Fragoso, C.R.; Ruiz-Armenteros, A.M.; Cabral, J.J.D.S.P.; Montenegro, S.M.G.L. Uncertainties Involved in the Use of Thresholds for the Detection of Water Bodies in Multitemporal Analysis from Landsat-8 and Sentinel-2 Images. *Sensors* **2021**, *21*, 7494. [CrossRef]
52. Towers, P.C.; Poblete-Echeverría, C. Effect of the Illumination Angle on NDVI Data Composed of Mixed Surface Values Obtained over Vertical-Shoot-Positioned Vineyards. *Remote Sens.* **2021**, *13*, 855. [CrossRef]

53. Tavora, J.; Gonçalves, G.A.; Fernandes, E.H.; Salama, M.S.; Van Der Wal, D. Detecting Turbid Plumes from Satellite Remote Sensing: State-of-Art Thresholds and the Novel PLUMES Algorithm. *Front. Mar. Sci.* **2023**, *10*, 1215327. [CrossRef]
54. Xiong, Q.; Wang, Y.; Liu, D.; Ye, S.; Du, Z.; Liu, W.; Huang, J.; Su, W.; Zhu, D.; Yao, X.; et al. A Cloud Detection Approach Based on Hybrid Multispectral Features with Dynamic Thresholds for GF-1 Remote Sensing Images. *Remote Sens.* **2020**, *12*, 450. [CrossRef]
55. Tramutoli, V. *Robust AVHRR Techniques (RAT) for Environmental Monitoring: Theory and Applications*; Cecchi, G., Zilioli, E., Eds.; SPIE: Bellingham, WA, USA, 1998; Volume 3496, pp. 101–113.
56. Tramutoli, V. Robust Satellite Techniques (RST) for Natural and Environmental Hazards Monitoring and Mitigation: Theory and Applications. In Proceedings of the 2007 International Workshop on the Analysis of Multi-temporal Remote Sensing Images, Leuven, Belgium, 18–20 July 2007; pp. 1–6.
57. Filizzola, C.; Cerra, D.; Corrado, R.; de la Cruz, A.; Pergola, N.; Tramutoli, V. Robust Satellite Techniques (RST) for Pipeline Network Monitoring. In Proceedings of the 2007 International Workshop on the Analysis of Multi-temporal Remote Sensing Images, Leuven, Belgium, 18–20 July 2007; pp. 1–5.
58. Filizzola, C.; Corrado, R.; Marchese, F.; Mazzeo, G.; Paciello, R.; Pergola, N.; Tramutoli, V. RST-FIRES, an Exportable Algorithm for Early-Fire Detection and Monitoring: Description, Implementation, and Field Validation in the Case of the MSG-SEVIRI Sensor. *Remote Sens. Environ.* **2017**, *192*, e2–e25. [CrossRef]
59. Falconieri, A.; Colonna, R.; Di Leo, V.E.; Filizzola, C.; Mazzeo, G.; Pergola, N.; Pietrapertosa, C.; Tramutoli, V. Early Fire Detection with Higher Sensitivity and Timeliness: Porting the RST-FIRES Algorithm to Rapid Scan Geostationary Data. *Remote Sens.* **2026**, *18*, 1861. [CrossRef]
60. Colonna, R.; Filizzola, C.; Di Leo, V.E.; Mancusi, I.; Lisi, M.; Tramutoli, V. High-Resolution Burned Area Mapping Using Sentinel-2 Imagery and Robust Satellite Techniques. *Remote Sens.* **2026**, *18*, 3494. [CrossRef]
61. Casciello, D.; Lacava, T.; Pergola, N.; Tramutoli, V. Robust Satellite Techniques for Oil Spill Detection and Monitoring Using AVHRR Thermal Infrared Bands. *Int. J. Remote Sens.* **2011**, *32*, 4107–4129. [CrossRef]
62. Grimaldi, C.S.L.; Casciello, D.; Coviello, I.; Lacava, T.; Pergola, N.; Tramutoli, V. An Improved RST Approach for Timely Alert and Near Real Time Monitoring of Oil Spill Disasters by Using AVHRR Data. *Nat. Hazards Earth Syst. Sci.* **2011**, *11*, 1281–1291. [CrossRef]
63. Pergola, N.; Marchese, F.; Tramutoli, V. Automated Detection of Thermal Features of Active Volcanoes by Means of Infrared AVHRR Records. *Remote Sens. Environ.* **2004**, *93*, 311–327. [CrossRef]
64. Marchese, F.; Filizzola, C.; Genzano, N.; Mazzeo, G.; Pergola, N.; Tramutoli, V. Assessment and Improvement of a Robust Satellite Technique (RST) for Thermal Monitoring of Volcanoes. *Remote Sens. Environ.* **2011**, *115*, 1556–1563. [CrossRef]
65. Tramutoli, V.; Cuomo, V.; Filizzola, C.; Pergola, N.; Pietrapertosa, C. Assessing the Potential of Thermal Infrared Satellite Surveys for Monitoring Seismically Active Areas: The Case of Kocaeli (Izmit) Earthquake, August 17, 1999. *Remote Sens. Environ.* **2005**, *96*, 409–426. [CrossRef]
66. Genzano, N.; Filizzola, C.; Hattori, K.; Pergola, N.; Tramutoli, V. Statistical Correlation Analysis Between Thermal Infrared Anomalies Observed from MTSATs and Large Earthquakes Occurred in Japan (2005–2015). *J. Geophys. Res. Solid Earth* **2021**, *126*, e2020JB020108. [CrossRef]
67. Filizzola, C.; Corrado, A.; Genzano, N.; Lisi, M.; Pergola, N.; Colonna, R.; Tramutoli, V. RST Analysis of Anomalous TIR Sequences in Relation with Earthquakes Occurred in Turkey in the Period 2004–2015. *Remote Sens.* **2022**, *14*, 381. [CrossRef]
68. Peleli, S.; Kouli, M.; Vallianatos, F. Satellite-Observed Thermal Anomalies and Deformation Patterns Associated to the 2021, Central Crete Seismic Sequence. *Remote Sens.* **2022**, *14*, 3413. [CrossRef]
69. Guo, A.; Jiang, N.; Xu, Y.; Xu, T.; Wu, Y.; Li, S.; Gao, Z. Co-Seismic Characterization Analysis in PWV and Land-Atmospheric Observations Associated with Luding Ms 6.8 Earthquake Occurrence in China on September 5, 2022. *Geomat. Nat. Hazards Risk* **2023**, *14*, 2279494. [CrossRef]
70. Huang, Y.; Cui, J.; Zhima, Z.; Jiang, D.; Wang, X.; Wang, L. Construction of a Fine Extraction Process for Seismic Methane Anomalies Based on Remote Sensing: The Case of the 6 February 2023, Türkiye–Syria Earthquake. *Remote Sens.* **2024**, *16*, 2936. [CrossRef]
71. Chao, J.; Zhao, Z.; Lai, Z.; Liu, J.; Hu, Y.; Cui, D. Exploring Geothermal Potential with Robust Satellite Techniques Using MODIS LST Data. *Geothermics* **2025**, *132*, 103414. [CrossRef]
72. Jing, F.; Chauhan, A.; Raju, A.; Singh, R.P. Changes in Land, Ocean, Atmospheric Parameters Associated with the 2025 Myanmar (Mw 7.7) Earthquake. *Geomat. Nat. Hazards Risk* **2026**, *17*, 2649431. [CrossRef]
73. Filizzola, C.; Carlucci, M.A.; Genzano, N.; Ciancia, E.; Lisi, M.; Pergola, N.; Ripullone, F.; Tramutoli, V. Robust Satellite-Based Identification and Monitoring of Forests Having Undergone Climate-Change-Related Stress. *Land* **2022**, *11*, 825. [CrossRef]
74. Lea, J.M. From Ice Sheet to Ocean: Local to Global Impacts of Arctic Iceberg Hazards. In *Glaciers Ice Sheets Warm. World Impacts Outcomes*; Drewry, D.J., Ed.; United Kingdom National Commission for UNESCO: London, UK, 2025; pp. 84–87.
75. Howell, S.E.L.; Babb, D.G.; Landy, J.C.; Brady, M. Multi-Year Sea Ice Conditions in the Northwest Passage: 1968–2020. *Atmos.-Ocean* **2023**, *61*, 202–216. [CrossRef]

76. Van Wyk de Vries, M.; Lea, J.M.; Ashmore, D.W. Crevasse Density, Orientation and Temporal Variability at Narsap Sermia, Greenland. *J. Glaciol.* **2023**, *69*, 1125–1137. [CrossRef]
77. Marzocchi, A.; Hirschi, J.J.-M.; Holliday, N.P.; Cunningham, S.A.; Blaker, A.T.; Coward, A.C. The North Atlantic Subpolar Circulation in an Eddy-Resolving Global Ocean Model. *J. Mar. Syst.* **2015**, *142*, 126–143. [CrossRef]
78. Florindo-López, C.; Bacon, S.; Aksenov, Y.; Chafik, L.; Colbourne, E.; Holliday, N.P. Arctic Ocean and Hudson Bay Freshwater Exports: New Estimates from Seven Decades of Hydrographic Surveys on the Labrador Shelf. *J. Clim.* **2020**, *33*, 8849–8868. [CrossRef]
79. Allan, D.; Allan, R.P. Influence of Meltwater from Labrador Sea Ice and Icebergs Transported Via the Flemish Cap on the Long-Term North Atlantic Cold Anomaly. *Atmos.-Ocean* **2025**, *63*, 21–38. [CrossRef]
80. Robe, R.Q.; Maier, D.C.; Russell, W.E. Long-Term Drift of Icebergs in Baffin Bay and the Labrador Sea. *Cold Reg. Sci. Technol.* **1980**, *1*, 183–193. [CrossRef]
81. Cook, A.; Dawson, J.; Holloway, J.; Milton, M.; Tagalik, S.; Baker, K.; Muckpah, J.; Elverum, S.; Boyse, E.; Clark, M.S.; et al. Implications of Changing Shipping Patterns near Communities across Arctic Canada. *Reg. Environ. Change* **2026**, *26*, 112. [CrossRef]
82. Mudryk, L.R.; Derksen, C.; Howell, S.; Laliberté, F.; Thackeray, C.; Sospedra-Alfonso, R.; Vionnet, V.; Kushner, P.J.; Brown, R. Canadian Snow and Sea Ice: Historical Trends and Projections. *Cryosphere* **2018**, *12*, 1157–1176. [CrossRef]
83. Copland, L.; Dawson, J.; Tivy, A.; Delaney, F.; Cook, A. Changes in Shipping Navigability in the Canadian Arctic between 1972 and 2016. *FACETS* **2021**, *6*, 1069–1087. [CrossRef]
84. Woodworth-Lynas, C.M.T.; Simms, A.; Rendell, C.M. Iceberg Grounding and Scouring on the Labrador Continental Shelf. *Cold Reg. Sci. Technol.* **1985**, *10*, 163–186. [CrossRef]
85. International Ice Patrol. *International Ice Patrol (IIP) Iceberg Sightings Database, Version 1*; National Snow and Ice Data Center: Boulder, CO, USA, 1995. [CrossRef]
86. Sentinel-2A: Extended Campaign Starting March 13, 2025. Available online: https://sentinels.copernicus.eu/-/sentinel-2a-extended-campaign-starting-march-13-2025 (accessed on 22 July 2026).
87. Kwong, I.H.Y.; Wong, F.K.K.; Fung, T. Automatic Mapping and Monitoring of Marine Water Quality Parameters in Hong Kong Using Sentinel-2 Image Time-Series and Google Earth Engine Cloud Computing. *Front. Mar. Sci.* **2022**, *9*, 871470. [CrossRef]
88. Google Earth Engine. Available online: https://earthengine.google.com (accessed on 22 September 2026).
89. Di Polito, C.; Ciancia, E.; Coviello, I.; Doxaran, D.; Lacava, T.; Pergola, N.; Satriano, V.; Tramutoli, V. On the Potential of Robust Satellite Techniques Approach for SPM Monitoring in Coastal Waters: Implementation and Application over the Basilicata Ionian Coastal Waters Using MODIS-Aqua. *Remote Sens.* **2016**, *8*, 922. [CrossRef]
90. Colonna, R.; Dal Sasso, S.F. Multi-Decadal Coastal Erosion Assessment and Machine Learning-Based Forecasts from Multi-Mission Satellites: Application to the Ionian Coast of Basilicata (1984–2050). *Geographies* **2026**, *6*, 20. [CrossRef]
91. Smith, W.D.; Dunning, S.A.; Brough, S.; Ross, N.; Telling, J. GERALDINE (Google Earth Engine supRaglAciaL Debris Input dEtector)—A New Tool for Identifying and Monitoring Supraglacial Landslide Inputs. *Earth Surf. Dyn.* **2020**, *8*, 1053–1065. [CrossRef]
92. Mohsen, A.; Fleit, G.; Kiss, T.; Baranya, S. Decoding Spatiotemporal Dynamics of Suspended Sediment and Vegetation in Shallow Reservoirs with Sentinel-2 and ANNs: A Case Study of Lake Tisza, Hungary. *Environ. Monit. Assess.* **2025**, *197*, 1249. [CrossRef]
93. Iceberg—Size, Shape, Types | Britannica. Available online: https://www.britannica.com/science/iceberg/Iceberg-size-and-shape (accessed on 22 July 2026).
94. Mobley, C. *Light and Water: Radiative Transfer in Natural Waters*; Academic Press: Cambridge, MA, USA, 1994.
95. Lee, Z.; Du, K.; Arnone, R.; Liew, S.; Penta, B. Penetration of Solar Radiation in the Upper Ocean: A Numerical Model for Oceanic and Coastal Waters. *J. Geophys. Res. Oceans* **2005**, *110*, 2004JC002780. [CrossRef]
96. Kara, A.B.; Wallcraft, A.J.; Hurlburt, H.E. A New Solar Radiation Penetration Scheme for Use in Ocean Mixed Layer Studies: An Application to the Black Sea Using a Fine-Resolution Hybrid Coordinate Ocean Model (HYCOM)*. *J. Phys. Oceanogr.* **2005**, *35*, 13–32. [CrossRef]
97. Lee, Z.; Hu, C.; Shang, S.; Du, K.; Lewis, M.; Arnone, R.; Brewin, R. Penetration of UV-visible Solar Radiation in the Global Oceans: Insights from Ocean Color Remote Sensing. *J. Geophys. Res. Oceans* **2013**, *118*, 4241–4255. [CrossRef]
98. International Regulations for Preventing Collisions at Sea, 1972. Available online: https://www.imorules.com/COLREG90_RULES.html#google_vignette (accessed on 7 October 2026).
99. International Maritime Organization. *International Convention for the Safety of Life at Sea (SOLAS), 1974*; International Maritime Organization: London, UK, 1974.
100. International Maritime Organization. *Guidelines for Voyage Planning*; Resolution A.893(21), adopted on 25 November 1999; International Maritime Organization: London, UK, 1999.
101. Rodriguez-Diaz, E.; Alcaide, J.I.; Endrina, N. Shadow Fleets: A Growing Challenge in Global Maritime Commerce. *Appl. Sci.* **2025**, *15*, 6424. [CrossRef]

102. Tramutoli, V. *Robust Satellite Techniques (RST) for Natural and Environmental Hazards Monitoring and Mitigation: Ten Year of Successful Applications*; IEEE: New York, NY, USA, 2005; Volume XXXVI-(7/W20), pp. 792–795.
103. Marchese, F.; Ciampa, M.; Filizzola, C.; Lacava, T.; Mazzeo, G.; Pergola, N.; Tramutoli, V. On the Exportability of Robust Satellite Techniques (RST) for Active Volcano Monitoring. *Remote Sens.* **2010**, *2*, 1575–1588. [CrossRef]
104. Sviashchennikov, P.; Drugorub, A. Long-Term Trends in Total Cloud Cover in the Arctic Based on Surface Observations in 1985–2020. *Bull. Geogr. Phys. Geogr. Ser.* **2022**, *22*, 33–43. [CrossRef]
105. Koeppen, W.C.; Pilger, E.; Wright, R. Time Series Analysis of Infrared Satellite Data for Detecting Thermal Anomalies: A Hybrid Approach. *Bull. Volcanol.* **2011**, *73*, 577–593. [CrossRef]
106. Landsat 8 | U.S. Geological Survey. Available online: https://www.usgs.gov/landsat-missions/landsat-8 (accessed on 22 July 2026).
107. Genzano, N.; Colonna, R. 3D Thermal Volume Mapping to Assess the Biological and Physical Characteristics of Olive Crops Using Remote Sensing and Photogrammetric Methods. *Appl. Geomat.* **2026**, *18*, 6. [CrossRef]
108. Seaman, C.; Hillger, D.W.; Kopp, T.; Williams, R.; Miller, S.; Lindsey, D. *Visible Infrared Imaging Radiometer Suite (VIIRS) Imagery Environmental Data Record (EDR) User's Guide*; Version 1.3; NOAA: Silver Spring, MD, USA, 2015. [CrossRef]
109. NASA. Visible Infrared Imaging Radiometer Suite (VIIRS). Available online: https://www.earthdata.nasa.gov/data/instruments/viirs (accessed on 22 July 2026).

Disclaimer/Publisher's Note: The statements, opinions and data contained in all publications are solely those of the individual author(s) and contributor(s) and not of MDPI and/or the editor(s). MDPI and/or the editor(s) disclaim responsibility for any injury to people or property resulting from any ideas, methods, instructions or products referred to in the content.